Tidal currents in the St. Lawrence Island region

Seth Danielson[1]

Zygmunt Kowalik*[1]

[1]Institute of Marine Science, University of Alaska Fairbanks, Fairbanks, Alaska, USA

*corresponding author: ffzk@ims.uaf.edu

An edited version of this paper was published by AGU.

Citation: Danielson, S.; Kowalik, Z.; (2005), *Tidal currents in the St. Lawrence Island region,* J. Geophys. Res., Vol. 110, No. C10, C10004, 10.1029/2004JC002463

Keywords: Bering Sea, tidal currents, spatial and temporal variability, bottom boundary layer

Running Title: DANIELSON AND KOWALIK: ST. LAWRENCE IS. TIDAL CURRENTS

Abstract:

Vertical and spatial variability of tidal currents in the northern part of the Bering Sea near St. Lawrence Island were examined using observations made at 17 new and historical current meter mooring locations. The semi-diurnal currents dominate over the diurnal currents. Semi-diurnal currents exhibit a seasonal modulation with currents being somewhat stronger during the summer and fall when the density structure displays two-layer stratification. Diurnal currents exhibit a weak semi-annual modulation. Examination of the vertical structure of tidal currents shows that maximum semidiurnal currents are observed in the upper or middle layers down to a depth of about 20 m and below this depth the energy of the semidiurnal currents decreases rapidly. However, the energy of diurnal band currents remains almost constant with depth, decreasing only in close proximity to the bottom. Rotary spectral analysis applied to the records shows further differences: the M_2 clockwise (CW) component of rotation dominates in the upper and middle water column but the counterclockwise component (CCW) dominates near the bottom. Interpretation of these observed results points to the different bottom boundary layers (BBL) for the CW and CCW motions in addition to the role of density stratification in organizing the BBL. We compare results of a vertically averaged 2-d model to the observationally derived tidal ellipse parameters and show that the barotropic formulation provides a first-order description of the tidal regime within the domain.

1. Introduction

Until now only a handful tidal current measurements have been reported from the northern Bering Sea [Pearson et al., 1981; Mofjeld, 1984]. In this paper we utilize these historical records as well as newly available current meter data from the vicinity of St. Lawrence Island in attempt to construct the spatial and temporal variability associated with tidal currents around this island. St. Lawrence Island is situated on the Bering Sea shelf (Figure 1) about 250 km south of Bering Strait and 500 km northeast of the shelf break.

An encompassing oceanographic background for the Bering Sea shelf, including discussion of tides, hydrography, circulation, ice and meteorology, is given by Hood and Calder [1981]. Fall storms tend to mix and cool the water column until by December the northern shelf waters are vertically homogeneous and at the freezing point. Ice cover progresses from north to south [Niebauer et al., 1999] and by the end of December the entire northern shelf is ice covered. During the winter, a polynya is generated immediately to the south of St. Lawrence Island by periodic strong northerly wind events [Schumacher et. al., 1983; Johnson and Kowalik, 1986]. Opening and closing of the polynya occurs until late April, when increasing solar radiation and warmer air temperatures melt the sea ice. Spring and summer insolation, the fresh ice melt and the spring river freshets progressively stratify the water column so that by the end of summer the northern shelf is essentially a two layer fluid: a homogeneous lower layer of cold, salty water remnant from the previous winter (mixed by tidal currents) and a homogeneous upper layer (mixed by winds) comprised of relatively fresh and warm waters. Surface cooling and fall storms then break down this stratification and the cycle begins anew. The unique location of the northern Bering Sea as a transition zone between the mid-latitudes and the Arctic results in three different water types (Alaska Coastal Water, Bering Shelf Water and Anadyr Water [Coachman et. al., 1975]) that pass

through Bering Strait to their eventual fate in the layers of the Arctic Ocean. The basic physical environment annual cycle of the northern Bering Sea region is depicted in Table 1.

Tides are an important and consistent driving force in the Bering Sea. Over the southeast Bering Sea shelf, where shoaling and/or resonance effects in Bristol Bay dominate, up to 90% of the kinetic energy is of tidal origin. According to Coachman [1986], in the St. Lawrence Island region tides account for only 10-40% of the total kinetic energy. Tide waves enter the Bering Sea as progressive waves from the North Pacific Ocean, mainly through the central and western passages of the Aleutian-Komandorski Islands [Sünderman, 1977; Pearson et al., 1981; Kantha, 1995]. The Arctic Ocean is a minor secondary source of tides, and therefore tides in the northern Bering Sea are considered to be the result of co-oscillation with the Pacific and, to a lesser degree, with the Arctic Ocean. Pearson et al. [1981] constructed empirical charts for four major tidal constituents (M_2, N_2, K_1, and O_1) over the Bering Sea shelf. Mofjeld [1984, 1986] and Mofjeld et al. [1984] analyzed data for three diurnal components (O_1, P_1, K_1) and three semidiurnal components (M_2, S_2, N_2) over the northeastern Bering shelf and made comparisons against numerical models and tidal theory. Observations show that over most of the shelf regions, the tides are primarily semidiurnal. However, near some of the Aleutian Islands, in Norton Sound and at some locations along the shelf break, diurnal tides can be dominant. The tides on the northeastern Bering Sea shelf are in a transitional regime, between low tides north of Bering Strait and high tides along the Bering shelfbreak.

The major semidiurnal constituent M_2 displays approximately 20 cm amplitude near St. Lawrence Island. The M_2 tide is under the influence of amphidromic systems located near Bering Strait, southeast of St. Lawrence Island and in the Gulf of Anadyr [Kowalik, 1999]. The dynamics of diurnal tides can be described using the major constituent K_1. K_1 wave has a maximum

amplitude of approximately 40 cm in the region of the shelf break and this amplitude decreases from the shelf break to about 7-8 cm in the St. Lawrence Island region, thus indicating the presence of trapped shelf waves [Baines et al., 2004]. Mofjeld [1984] suggested that such behavior of the K_1 tidal wave on the Bering Sea shelf resembles a Sverdrup wave generated by an incident wave from the deep Bering basin. The Sverdrup wave model predicts well the amplitudes and phases of the tides on the Bering Sea shelf. These waves, in a frictionless ocean below the critical latitude (for K_1 tide, $\Phi = 30^{\circ}$), propagate as free waves; above this latitude they change to subinertial evanescent waves. Data described by Mofjeld [1986] from the northwestern shelf show that the tidal harmonic constants change seasonally. The diurnal amplitude increased and semidiurnal amplitude decreased during winter. The increase and decrease amounted to a few percent of the mean values. The maximum change in amplitude is close to 3 cm and the maximum change in phase is up to 15° for the M_2 tide in Bering Strait. The relatively large changes in amplitude (37% of the mean amplitude) at this site possibly expresses damping of the tides by ice in the Arctic Ocean [Kowalik and Proshutinsky, 1994].

Five current meter stations located near St. Lawrence Island were described by Pearson et al. [1981] and Mofjeld [1984]. For comparison to the observations newly available to this study, the moorings deployed in the 1970s and 1980s (NC19B, NC25A, NC26B, LD2 and LD3) are reproduced in Table 2 and Table 3. These historical measurements give broader spatial coverage than the newer observations but none of the historical records were made over the course of an entire calendar year or over the entire water depth.

Here we report on tidal analyses from twelve additional year-long stations in the vicinity of St. Lawrence Island. The objectives of this paper are (a) to examine the temporal and spatial variations of the observed tidal currents, (b) to compare the observed currents with the calculated

barotropic currents of a numerical model, (c) to investigate rotational spectra and the vertical distribution of tidal currents within the water column and (d) to apply bottom boundary layer (BBL) theory for an explanation of the observed structure of the tidal current characteristics within the water column. This paper is organized in the following way. In Section 2 the tidal currents are examined using harmonic analyses and tidal current ellipses are compared to the results from the vertically averaged model. Seasonal and vertical variability in the tidal currents is described in Section 3, including rotary spectra analysis to discern different behavior of the semidiurnal and diurnal components. Interpretation of the observations with the help of simple equations for the BBL in a rotational, density stratified flow is given in Section 4. Section 5 provides discussion and concluding remarks. In Appendix A, a basic set of equations for the BBL is briefly described.

2. Spatial distribution of tidal currents

2.1 Observations

Twelve moorings were deployed to collect velocity data at hourly intervals over the period of one year from September 1998 to September 1999. Figure 1 shows a detailed map of the St. Lawrence Island region with these mooring locations and the five historical mooring locations taken from Pearson et al. [1981] and Mofjeld [1984]. Table 2 summarizes the mooring names, instrument types, spatial coordinates, current meter depths, water column depths and record lengths for the data sets employed.

Recently deployed moorings utilized RD Instruments 300 KHz Acoustic Doppler Current Profilers (ADCPs) and Aanderaa RCM4 and RCM7 current meters. Linear interpolation between pre- and post- calibrations were applied to RCM data sets when possible. All records were corrected for clock drift when possible then interpolated with cubic splines to the top of each hour.

RCM data was likely subject to some degree of jellyfish biofouling. The records that appeared to be affected primarily were P1 in February, P2 during summer months, FTS8 in winter, the upper instrument at H1 in late summer, and intermittently at H3 and H4. Comparison of speed distributions to the nearby ADCP instruments and other RCM instruments leads us to believe that the periods of intermittent rotor stalls have only a minor effect on the outcome of our harmonic fits, in part because of the averaging employed. ADCP derived velocities were corrected for speed of sound at the transducer head based on a salinity value measured by a nearby T/C recorder and temperature measured by the ADCP. In addition, the following quality control criteria were applied to the ADCP data: data failing any of the following tests were rejected. A) Data determined to be in bins above the sea surface. B) Data within the beam side-lobe reflection shadow. C) Correlation of less than 64% on any one beam. D) Percent-good 4-beam solutions <10%. E) Percent-good 4-beam solutions + percent-good 3-beam solutions <20. Hour-long ADCP ensembles collected 105 pings per ensemble so upon application of the above screening parameters, the standard deviation of each ADCP measurement is between 0.6 and 1.3 cm/s.

Analysis software T-TIDE by Pawlowicz et al. [2002], was used for all tidal harmonic fit computations. New results given in Tables 3a and 3b have been computed in a consistent manner to these historical analyses for ease of comparison. The essence of this analysis approach is consecutive 29-day harmonic analyses spaced every 15 days from the beginning of the record. Three rows are dedicated to each ADCP mooring: one near-surface depth, one near-bottom depth and the vertical average. Tidal ellipse parameters were not recomputed for the historical records. Rather, we have taken the previously published findings for these moorings [Pearson et al., 1981; Mofjeld, 1984], adjusting the inclination (and phase when necessary) to conform to the current standard of reporting ellipse inclination with respect to due east. Results from moorings LD2 and

LD3 were published with one month of data so the standard deviation entry in Table 3 is blank for these moorings. Moorings LD2 and LD3 represent mid-summer conditions; NC19B, NC25A and NC26A represent tidal currents from the November through June time frame. See Table 1 and the discussion below for ramifications of these temporally restricted sample periods.

The record-length analyses show that the M_2 constituent contains the most energy, with current speeds between 3.1 and 16.0 cm/s. K_1 is the largest diurnal constituent, with current speeds between 1.8 and 7.5 cm/s. For records with an entire years worth of data, the M_2 (K_1) current speed maxima and minima are 16.0 (4.1) and 6.2 (2.0) cm/s respectively. At ADCP mooring F8, vertically averaged M_2 and K_1 are 14.3 cm/s and 3.9 cm/s respectively; the third through tenth largest resolved constituents are all in the range between 1.2 and 3.7 cm/s. The first ten constituents at this mooring, in order of magnitude, are M_2, K_1, N_2, MM, MSM, MF, 0_1, S_2, SSA and P_1. All ten constituents have a signal to noise ratio greater than 2. The sum of these first ten amplitudes is about 38 cm/s. The mean current speed of a year-long tidal prediction that includes all resolved constituents is about 12 cm/s. Larger standard deviations of the diurnal constituent K_1 may reflect the difficulties in resolving K_1 from P_1 in the month long analysis even with the use of inference or may be an indication of the lower signal to noise ratio for K_1. Propagation of the time of maximum M_2 and K_1 currents generally progresses from east to west for the region to the south of the island with the notable exception of mooring H5 off Southeast Cape. The three moorings located off Chibukak, Northeast and Southeast Capes have the three largest Greenwich phase values, indicating that these promontories may act to disrupt the wave propagation.

2.2 Vertically-integrated model

We compare tidal current ellipses from the measurements to the output of a tidal model constructed around St. Lawrence Island. The model employs a spatial resolution of approximately 1.85 km and the boundary conditions for the local model were taken from a large scale model of the entire Bering Sea. The formulation, mechanics and performance of the model are described in detail in Kowalik [1999].

The ellipses for the M_2 tide are shown in Figure 2 and ellipses for the K_1 tide are shown in Figure 3. Ellipse parameters from the model grid points closest to the mooring locations are also given in Tables 3a and 3b. We applied two-sided t-tests to determine 95% confidence bounds for each of the observed ellipse parameters, assuming that the number of degrees of freedom is equivalent to the number of months sampled. Confidence limits computed in this fashion provide similar results to those given by the T-TIDE package. Modeled ellipse parameters that fall within the 95% confidence limits are shaded in boldface type within Tables 3a and 3b. We are unable to construct confidence limits for historical moorings LD2 and LD3 because only one month of data was reported. Semi-minor axes for which the confidence limits cross zero indicates uncertainty in the direction of rotation and is reflected in appropriate shading of the rotation direction.

For the M_2 constituent, the mean magnitude of difference between the observed and modeled ellipse parameters given in Table 3 are: semi-major axis = 3.2 cm/s, semi-minor axis = 1.4 cm/s, inclination = 17º, and phase = 18º. For the K_1 constituent, the differences are: semi-major axis = 1.2 cm/s, semi-minor axis = 0.5 cm/s, inclination = 18º, and phase=19º. Many of the inclination and phase angles for both constituents are resolved to within 10º of the observations even when they do not fall within the 95% confidence limits. The model resolves the semi-major current speeds nearly equally well for the two constituents (M_2 mean error = 33%; K_1 mean error = 43%), expressed as a fraction of the RMS error to the mean amplitude of the observed semi-major

axis. Based on the confidence limits, the model fully or nearly resolves both M_2 and K_1 currents at some sites (e.g., P1-F5 and H4), but has trouble at other nearby locations (e.g., F6 and NC25A). The M_2 transition from counterclockwise (CCW) rotation just south of the island to clockwise (CW) rotation farther south places F6 and NC25A in a transitional regime with nearly degenerate ellipses. At F6, the model underestimates the M_2 vertically averaged currents by 6 cm/s, although only 15 km away the model predicts a semi-major axis that is within 1 cm/s of the F6 current. With its high horizontal resolution the model has the ability to resolve a wide dynamic range over a short spatial scale, underscoring the importance of having an accurate bathymetric grid. The larger standard deviation of phase at some sites (e.g., F6 for M_2 at 37 m) is an indication that the tidal signal can be nonstationary. To fully resolve the tidal currents at such locations may require in part a model that includes physics beyond the vertically averaged case (e.g., inclusion of seasonally varying density structure - see sections 3 and 4 for further development of this aspect).

The three historical measurements to which we can make a statistical comparison fare poorly compared to more recent measurements: none of the semi-major axes fall within the confidence limits, and only a few of the other parameters are resolved. Historical M_2 semi-major currents, with the exception of LD2, are smaller than the computed ellipses. Mooring NC25A has only half the semi-major axis M_2 amplitude of moorings F8 and F4 (spaced < 40 km apart) even though it was located midway between these two other sites and in a region of gently sloping bottom relief. Similar differences at NC25A are seen in the diurnal constituent. Perhaps the other historical results are suspect as well, but we have no other mooring results to provide another perspective at or near these locations. Rather than rejecting any ellipse parameters as necessarily faulty, we leave it to the reader to make their own assessment of the utility of the model results and/or observed parameters.

Divergence between the modeled and observed ellipse parameters may be due in part to 1) inaccurate bathymetric grid employed by the model, 2) density structure is absent from the model, 3) location of the recording instrument within the bottom boundary layer (often so placed to observe dense water and to avoid winter ice keels) and 4) the mismatch of comparison between a vertically averaged parameter and a measurement at one particular depth. We will show in Sections 3 and 4 that the latter three sources of uncertainty should be particularly strong for the M_2 constituent. The first source of uncertainty, deficiencies in our current realization of the true bottom relief, may be the most limiting factor to model accuracy for both constituents.

The resolved ellipse orientation is generally parallel to the bathymetric contours and ellipses are typically more rectilinear for locations closer to the shore and in the straits. The model delineates regions of stronger currents in the St. Lawrence Island domain, in particular off of Southeast Cape and to a lesser extent off of Chibukak and Northeast Capes. The stronger tidal currents of these locations are probably due to shallower bathymetry which conforms to the cape structure. It is interesting that Anadyr Strait, located between the island and Siberia, strongly controls the tidal motion both in the semidiurnal and diurnal bands by changing the flow from elliptical to rectilinear, whereas off of Northeast Cape in Shpanberg Strait K_1 appears much more elongated than M_2. The K_1 wave has approximately twice the wavelength of the M_2 wave so it is not surprising that the K_1 ellipses are less able to exhibit rotational character within the straits. The wider nature of Shpanberg Strait (approx. 200 km) apparently allows for more rotation of the M_2 wave than does Anadyr Strait (approx. 75 km). However, the model does not properly capture the low-eccentricity nature of the M_2 tide as observed at the easternmost two mooring locations. We ascribe these differences to the probable causes noted above and point out that approximately 25 km to the east of LD2 the model does predict more circular ellipses.

In summary, the spatial variability of the tidal ellipses over the course of our domain depict a dynamic region that is strongly influenced by the coastlines and bottom topography. Both M_2 and K_1 ellipses exhibit a range of speed that varies by factor of five and can be either highly rectilinear or have no eccentricity whatsoever. Despite the limitations inherent within both the vertically integrated model and the measurements, many computed ellipse parameters turned out to be in agreement with those obtained from the harmonic analyses, thus implying that a barotropic description provides a first-order estimate of the tidal regime in this region.

3. Structure of temporal and vertical variability

3.1 Mean vertical distribution

To examine the primary characteristics in the tidal current distribution along the vertical direction we describe yearlong analyses at mooring F8. Structure of the tidal currents through the water column based on the annual analysis for all depths at mooring F8 is shown in Figure 4. Confidence limits for the yearlong analyses are taken from the T-TIDE output. M_2 tidal currents are relatively constant (15 ±2 cm/s) from the surface down to approximately 15 m depth, depict a slight maximum around 20 m, and then decay to the instrument depth of 43 m. This character is seen in both the semi-major and semi-minor axes. The direction of rotation for the M_2 ellipse is negative (CW) and only in close proximity to the instrument the direction changes to positive rotation (CCW). This reflects that in the entire layer of decreasing current magnitudes, progressing toward the bottom, the sense of rotation tends more and more to the CCW direction. The M_2 current ellipse only slightly changes eccentricity in the surface layer, as both major and minor axes are relatively constant. Below 25 m, the eccentricity decreases until at about 10 m above the bottom the ellipse becomes rectilinear, indicative of the change in sense of rotation. The M_2 inclination

and phase both are constant in the upper 15 m of the water column then undergo a linear decrease of about 15º to the instrument depth.

In contrast to the M_2 currents, the K_1 tidal current semi-major and semi-minor axes are invariant over the course of the water column. The phase and inclination of K_1 progress from the surface to the instrument depth over a range of about 20º in an opposite sense to the change of the M_2 parameters. The diurnal BBL must be located below the deepest measurement depth, i.e., 6 m above the bottom. Mean variations through the water column are in the range of ±10º and ±0.5 cm/s. The direction of rotation for the K_1 ellipse does not change from CW throughout the measured water column.

3.2 Seasonal variability

For the two moorings with profiling ADCPs (F6 and F8), we also computed overlapping monthly tidal harmonic analyses for the year-long series at each depth bin. This allows us to assess the seasonal character in conjunction with the vertical structure for a comprehensive description of the tidal currents. Figure 5 describes the yearly cycle of the M_2 tidal currents from F8 and shows the development of a non-uniform vertical distribution of currents during the summer. The character of the M_2 tidal currents changes over the course of the year as the water column progresses between the cold, salty, ice covered winter conditions between January and March and the two-layer, sharply stratified conditions of July through September. For M_2, the time periods of October to December and May to June are transition periods between these two extremes. The main periodicity is a yearly cycle with weaker winter currents and stronger summer currents. The month-long analyses reveal that the M_2 currents varied from as little as 7 cm/s (near the bottom in the winter) to as much as 21 cm/s (near the surface in the summer). Minimum values were observed

near the bottom during all months, the smallest values occurring between January and March. Tidal currents were fairly constant between the surface and about 25 m during this time. During this period of ice cover, we do not see a near-surface boundary layer of tidal current attenuation similar to that observed near the bottom. This is one indication that the pack ice is not significantly influencing the tidal current profile.

During the stratified period (approximately June through September) at mooring F8 a subsurface maximum of the M_2 currents occurred between 20 and 25 m, whereas at F6 (just 20 km away) the M_2 currents are maximal at the surface and decay throughout the water column toward the bottom. From March to October, ellipse inclination and phase both are constant in the upper 20m and then decay from 20m to the bottom. This describes the tendency of ellipses, with decreasing distance to the bottom, to be aligned progressively more in the CCW sense. From November through April the phase and inclination have a smaller range of values through the water column.

The diurnal tidal currents are smaller than the M_2 currents and exhibit markedly different seasonal character. K_1 does not have an annual modulation. Constituent K_1 (T=23.934522 h) is not resolved from constituent P_1 (T= 24.065873 h) in a 29-day analysis, so instead P_1 was inferred from K_1 using the relationship determined by the yearlong analysis [Foreman and Henry, 1989; Pawlowicz et al., 2002]. Linear superposition of K_1 and P_1 creates a beat period of 1/2 year [Pugh, 1987]. In the St Lawrence Island region, the manifestation of this semi-annual period (Figure 6) results in approximately 2.5 cm/s difference between February/August (2.5 cm/s) and November/May (5 cm/s). Although 5 cm/s is not a particularly energetic flow, it is of the same order of the mean background flow (3.6 cm/s) at NC25A [Schumacher et al, 1983] and is approximately 40% of the annual mean tidal flow and 14% of the peak tidal flow. The major

seasonal cycle for the diurnal currents is not related to the annual cycle of density which dominates behavior of M_2, but the semi-annual cycle caused by the linear superposition of the K_1 and P_1 constituents. Beating of close constituents also occurs for semi-diurnal tides. We will show later that M_2 and N_2 exhibit a monthly beat that dominates the total tidal energy profiles.

3.3 Rotary spectra

Tidal current parameters were also evaluated based on rotary spectra analysis [Gonella, 1972; Mooers, 1973; Emery and Thomson, 2001]. Figure 7 depicts the rotary spectra for the 10 m and 43 m depths at mooring F8. This analysis shows that the energy of semidiurnal tides dominates both the upper and lower water column. The contribution of diurnal tides to the total energy is smaller, although the second strongest maximum in the energy spectra belongs to the K_1 tide. Tidal maxima show slight seasonal variability, but it is not the strongest feature of the tidal regime depicted by the rotary spectra.

The feature which sets apart the tidal currents in the upper and lower water column are the CW and CCW components of rotation. At 10 m depth, the energy of the CW component at the M_2 period is two to three times greater than the energy of the CCW component, while at 43 m depth the CCW component slightly dominates. The same behavior, i.e., prevalence of CW motion at the surface and growth of the CCW motion towards the bottom can be discerned for both seasons as well as the other semidiurnal tides, cf., S_2 and N_2. The ratio of CW to CCW energy (approximately 3.5) in the diurnal band does not appreciably change with depth or season.

The broad inertial oscillation maximum of CW currents (Figure 7c) exhibits strong seasonal variability. Amplification of near-inertial clockwise currents in the upper layer of the water column during the summer period is seen in this figure. Wind-generated motion supplies energy only

through the surface layer of the ocean in the wide frequency band around the inertial frequency. The strong summer stratification appears to limit the enhancement of near-inertial motion to the upper layer. Figure 7c also suggests that the summer enhancement is not limited to inertial motion, as the clockwise currents at the N_2 frequency have been magnified with respect to the N_2 currents shown in panel 7a. However, the noise floor of the semi-diurnal band in the near-surface winter spectrum (7a) appears depressed with respect to the other three spectra, so such characteristics are difficult to assess. In winter, there is no near-surface maximum in the power spectra around the inertial period of oscillation. One may be tempted to speculate that a possible cause of the diminished wintertime inertial-band energy is reduced air-sea coupling due to sea ice cover, but the vast majority of ice in the northern Bering Sea is in free drift and the wind stress is larger in the winter than in the summer. Maas and van Haren [1987] demonstrated a dramatic increase in energy of the inertial oscillations, in the central part of the North Sea, from the unstratified winter conditions to the stratified summer conditions, despite the lack of ice cover during the winter and the wind forcing during the two seasons is not significantly different.

We have described in Sections 3.1-3.3 the temporal and vertical structure of tidal currents at this one location on the northern Bering Sea shelf. In the next section we use numerical models to explain observed differences between the M_2 and K_1 currents.

4. BBL structure for the subinertial and superinertial tides

In this final section, the vertical velocity structure and rotational characteristics described previously will be examined numerically. We seek an explanation of the different behavior of the M_2 and K_1 currents through the water column by deconstructing the different BBL regimes for the subinertial and superinertial tides. We do this by outlining the pertinent BBL dynamics and then

looking into effects of density stratification and constant and variable eddy viscosity coefficients upon the CW and CCW rotating components of currents.

Equations for boundary layer dynamics, along with the analytical solutions are given in Appendix A. The BBL for the rotating (tidal) flow, although similar to the Ekman BBL concept, differs strongly in magnitude. The magnitude of the thickness δ of the BBL can be evaluated from the exponent in the solution (13a) derived in Appendix A, assuming decay of $e^{-\alpha_q \delta}$ and $e^{-\alpha_r \delta}$ is equal to e^{-1}.

$$\delta^{\pm} \simeq \sqrt{\frac{2N_z}{\omega \pm f}} \qquad (1)$$

Here N_z denotes the eddy viscosity coefficient, ω is the tidal frequency, and f is the Coriolis parameter. Negative signs represent clockwise rotation and positive signs represent counterclockwise rotation. At latitude 60ºN the disparity between the two scales at the M_2 frequency is quite strong, since $\delta^{-}/\delta^{+} \simeq 4$, but at the K_1 frequency this disparity diminishes to $\delta^{-}/\delta^{+} \simeq 2$. In Figure 8 the vertical distribution of the magnitude of velocity is shown for the CW and CCW motions, as obtained from the analytical solution (14a). Motion is considered in shallow water of 50 m depth and is imparted at the bottom by a circular current whose components for the clockwise motion are $u_0 \sin(\omega t)$ and $v_0 \cos(\omega t)$. The current magnitude is 10 cm/s and is equal to $\sqrt{(u_0^2 + v_0^2)}$. We consider circular motion so that the input into CW and CCW motion is the same and therefore the differences in the boundary layer thickness are not induced by unequal forcing.

The first case considered is with constant eddy viscosity set to 50 cm^2/s and the latitude set to 60ºN. The M_2 and K_1 velocity profiles are generated with circular motion imparted at the

seafloor (Figure 8). Profiles of the CW motion and CCW motion are both forced with the same magnitude. Strong disparity in the behavior of the CW and CCW motion exists. Because the M_2 wave is located in the superinertial frequency domain and its period (T_{M_2} = 12.42 hr) is close to the inertial period ($T_i = 13.82$ hr), while the K_1 wave is located in the subinertial domain and its period (T_{K_1} = 23.93 hr) is much larger than the inertial period, the thickness of the BBL for M_2 flow is greater than for K_1 flow.

A few conclusions follow from Figure 8 and from the solution given in Appendix A. Comparison of the M_2 profiles shows that the dominant component of velocity at the free surface is rotating clockwise, while close to the bottom the CCW rotation is stronger. The relation between M_2 and K_1 components can be deduced from this figure as well. Large differences are between clockwise rotating currents: M_2 tends to dominate in the surface layer, but K_1 is stronger in the bottom layer.

As suggested by Prandle [1982] the properties of the BBL are further elucidated by the use of a variable eddy viscosity (see eqs. 17a to 20a in Appendix A). The results of this scheme, based upon turbulent energy closure, are not radically different from previous studies employing piecewise linear eddy viscosity [e.g., Fjeldstad, 1936; Maas and van Haren, 1987; Souza and Simpson, 1996; van Haren, 2000; Howarth, 1998]. To investigate the differences between constant and variable eddy viscosity coefficient the vertical exchange of momentum is first considered in a uniform (unstratified) water column. Results of numerical computations for this case are shown in Figure 9a, for the M_2 wave and 9b for the K_1 wave. All parameters are defined for the geometry considered in Figure 8. For comparison, previous results with constant eddy viscosity are given as well. The influence of the depth-dependent eddy viscosity is expressed in a narrowing of the BBL, both for the semidiurnal and diurnal tides and for the clockwise and counterclockwise rotations. As

before, the motion imparted at the bottom influences the higher levels of the water column mainly through the clockwise M_2 component. With a variable eddy viscosity, the magnitude of the CW component of M_2 current is still growing even at 50 m from the bottom. The CW motion in K_1 component reaches constant magnitude below the free surface. The vertical distribution of the eddy viscosity coefficient for the CW and CCW rotation of the M_2 wave is shown in Fig. 10. The velocity distribution given in Figure 9 influences the vertical distribution of the eddy viscosity. For CW motion the maximum value of the eddy viscosity is greater and is located higher in the water column than the maximum for CCW rotation.

A typical density profile south of St. Lawrence Island at the late summer shows very strong fresh water and solar heating influence (Figure 11a). The water column structure depicts two-layers of well-mixed density which are divided by a narrow pycnocline. The density stratification resulted in the new profile of the eddy viscosity (Figure 11b). Due to the density stratification, turbulence generated in the BBL has been strongly reduced and at about 20 m above the bottom it is completely damped. Therefore, the eddy viscosity changes only in the near-bottom region and above 20 m from the bottom the eddy viscosity is reduced to a constant, near zero value. Such distribution of the turbulence generates a velocity profile that has a small maximum at the bottom of the pycnocline and constant magnitude above (Figure 11c). The presence of a tidal current maximum for the M_2 constituent in the pycnocline region has been noticed in earlier observations [Fjeldstad, 1936] and the explanation invokes the dynamics of the rotational boundary layer in a stratified fluid [Maas and van Haren, 1987; Howarth, 1998 and van Haren, 2000].

The influence of the density stratification on the K_1 wave is negligible. The different behavior of the M_2 and K_1 waves is related to the different thickness of the BBL for these two waves. The boundary layer thickness of the K_1 wave is smaller than the distance to the pycnocline,

therefore the pycnocline region is encountered by the constant velocity profile without any gradients. On the other hand, the boundary layer for the M_2 wave is greater than the distance to the pycnocline. The M_2 wave profile exhibits a marked maximum in the pycnocline region. Since the CW constituent of M_2 has the largest thickness of the BBL it also depicts the strongest influence by the density stratification. Above the pycnocline the eddy viscosity is strongly damped, therefore in this region the vertical structure exhibits nearly constant velocity. This is in contrast to the velocity profile computed for the uniform density in the water column (cf. thick dashed line in Figure 9a). The key factor for the generation of different velocity profiles appears to be the location of the pycnocline in relation to the BBL. Both observations and theory point out that the changes in the vertical profiles will be dominated by the CW component of M_2 [Souza and Simpson, 1996; van Haren, 2000].

The above investigations were made for circular motion where the relative input of the CW and CCW motion was the same. To consider the possibility of generating an elliptical CCW motion in close proximity to the bottom by elliptical CW motion imparted at the surface we take the surface currents from the F8 mooring and use them as the forcing function for the boundary layer currents. In Figure 12 we compare the results of this final numerical experiment with the current ellipses observed at F8. We consider motion generated by the M_2 surface current whose components are $u_0 \cos(\omega t - g_u)$ and $v_0 \cos(\omega t - g_v)$. Amplitudes and phases of the current are: u_0 = 14.0 cm/s, g_u = 239.33º, v_0 = 5.3 cm/s, g_v = 88.90º. The density distribution for this computation is the same as in Figure 11. We point out that the actual density distribution at F8 for this period is unknown.

The M_2 tidal current ellipses have been plotted in Figure 12 at four levels (distances are given from the sea surface). In the surface layer (10 m), near the pycnocline (24 m), below the

pycnocline (36 m) and close to the bottom (44 m). While in the upper layer (10-15 m from the surface) the current ellipses conserve shape, magnitude, and sense of rotation. In the lower layer the ellipses change magnitude, shape and sense of rotation. The clockwise motion dominates in the entire water column with an exception of the narrow bottom layer where the M_2 current rotates counterclockwise. The decrease of the current towards the bottom is associated with the changes in the ellipse shape. Close to the bottom, due to the different decay rate of the CC and CCW components, the flow becomes more rectilinear. Especially interesting is the behavior of the tidal current ellipses in the pycnocline region where a maximum of the current occurs both in observation and model, although the model predicts smaller values than the observed ones.

5. Discussion and Summary

The main purpose of this study was to examine the tidal current regime in the vicinity of St. Lawrence Island. We aimed at explanation of the tidal velocities and their spatial and temporal variations through the water column, across the domain and in both the summer and winter seasons. The basic observations can be summarized as: (1) Semidiurnal currents dominate over diurnal currents. (2) Many tidal current parameter estimates from harmonic analyses are in agreement with parameters computed from a vertically integrated model, confirming the primarily barotropic nature of the currents. (3) The horizontal distribution of tidal currents is one of bathymetrically and frictionally steered current ellipses across the domain. Current speeds have a range of more than fivefold in both the M_2 and K_1 constituents. (4) Structure of the tidal currents through the water column is different for the semidiurnal and diurnal constituents. Semidiurnal currents change along the vertical direction while diurnal currents are nearly constant from just above the bottom to the free surface. (5) Rotary spectra analysis shows large differences in the diurnal and semidiurnal

tidal bands. The semidiurnal tides show prevalence of CW motion near the surface and growth of the CCW motion towards the bottom, whereas the ratio of CW and CCW energy in the diurnal tidal band does not change with depth.

We show that these peculiarities in the vertical behavior are related to the BBL in the tidal flow regime of approximately 50 m depth. Here we use an approach suggested by Visser et. al [1994]. Instead of the analytical solution for the two layer model which they used to examine tidal flow in very shallow (20 m) water, we use a numerical solution to the set of equations of motion together with turbulent closure models. This approach allows us to examine a tidally generated BBL in interaction with variable eddy viscosity. A similar approach to the investigations of the BBL was suggested by Marchuk and Kagan [1977] and Mofjeld et al. [1984]. Even the simplest model which describes tidally generated turbulence by constant eddy viscosity points out that the differences observed in the M_2 and K_1 velocity profiles are related to: (1) different frequency of oscillations and their relation to the inertial frequency, and (2) different sense of rotation (see eq. (1)). The BBL for the clockwise rotating M_2 currents extends from the bottom to the free surface, i.e., over the entire depth of the 50 m water column, while the BBL for the K_1 currents is limited to 15 m for CCW rotation and to 20 m for the CW rotation. Considerations with a variable eddy viscosity without density stratifications describe similar distributions of currents with a much thinner BBL, limited to 10 m, except for the CW rotating M_2 current whose BBL extends from the bottom to the surface.

Numerical experiments with two-layer density stratified flow shows that the only tidal mode interacting with the pycnocline is the one whose BBL is thicker than the distance from the bottom to the pycnocline. There is only one mode in our experiment set with such a large BBL, i.e., the semi-diurnal mode with CW rotation. Through interaction with the pycnocline, this wave

organizes a local maximum in the velocity distribution. M_2 is therefore the most likely constituent to induce vertical mixing by generating a region of enhanced velocity shear in the thermocline. Observations near St. Lawrence Island indicate that the change in the vertical profile of the semidiurnal tidal current is connected to the summer stratification (Figure 4). It follows from the rotary spectra (Figure 7) that at the same period a strong inertial motion develops. As processes of maintaining the summer stratification are controlled though a balance of tidal and inertial motion shear [van Haren, 2000] a picture of interaction between tides and inertial motion becomes more complicated. Vertical viscosity which modifies the tidal currents through dependence on stratification is related to the intensity of inertial motion as well.

Numerical computations based on observational data from mooring F8 help confirm the influence of the BBL on the tidal current distribution around St. Lawrence Island. The M_2 currents were computed in a stratified water column forced by the observed surface current. The resultant tidal currents show transformation from CW motion high in the water column to CCW motion in close proximity to the bottom. The observed disparity in the BBL regime of the diurnal and semidiurnal tides may be important for the understanding of exchange and transport processes driven by tides in close proximity to the bottom. Although semidiurnal currents dominate the dynamical processes at the ocean surface and at mid-depths, close to the bottom an exchange of mass and momentum may be driven by the diurnal currents.

The striking differences between diurnal currents which are nearly constant throughout the entire water column and decrease of the semidiurnal currents in the thick BBL are not limited to the Bering Sea or to other shallow seas of fresh water influence [Maas and van Haren, 1987; Visser at. al, 1994; Souza and Simpson, 1996], they were also observed in the southern Weddell Sea near the critical latitude by Foldvik et al. [1990]. At one of the mooring stations in the Weddell Sea the BBL

thickness of the CW and CCW components at M_2 frequency was estimated to differ by a factor of 15.

Unlike regions that experience shorefast ice where the surface tidal currents are very small due to an immobile boundary as observed by Sverdrup [1926], the observations near St. Lawrence Island are made below drifting sea ice. The amplitude of both the 10m M_2 and K_1 currents (Figure 7) do not appreciably change from summer to winter and the vertical distribution of the current magnitude (Figure 5) during winter shows very small near surface attenuation. Thus, the tidal waves are not significantly damped by sea ice cover. The pack ice of the northern Bering Sea is in free drift and it behaves as a flexible membrane which weakly damps vertical motion but resists horizontal convergence. Therefore, it tends to generate strong nonlinear motion. Observations of ice drift and deformation in the Bering Sea indicate nonlinear ice-water coupling in the tidal band of oscillations since the M_4 tidal component of the ice velocity is relatively much stronger than the M_4 in the ocean currents [Pease and Turet, 1989].

Following Maas and van Haren [1987] and Howarth [1998] we have excluded free internal tides as the source of changes in the tidal current distribution. The mooring stations around St. Lawrence Island were placed over smooth topography located about 500 km from the shelf break, where free internal tides are usually generated. Due to the intermittent character of the internal tides and the long distance of propagation from the likely source region to the mooring sites these waves will not be phase locked to the surface tides and therefore they will tend to be filtered out through the tidal analysis procedure.

Energy delivered to the system by tidal currents accounts for anywhere from less than 20% to greater than 80% of the total (Figure 13). The annual mean is close to 50%, larger than the expected mean of 10-40% given by Coachman [1986] for the region immediately to the south of St.

Lawrence Island. One reason for the previous underestimation of the fraction of kinetic energy due to tides is that the current meters were typically placed in close proximity to the bottom, in part to reduce risk from ice keels. Thus, the measurements have been located within the M_2 BBL and have underestimated semidiurnal currents. The tidal kinetic energy comes in packets with an approximately one month beat, the period of which is set up by superposition of semi-diurnal constituents M_2 and N_2. These packets have the greatest energy in the summer when a density modified semidiurnal tide is generated. The beating is also enhanced during periods of constructive interference between diurnal constituents K_1 and P_1, a process that undergoes a semi-annual modulation.

There exists potential for the effects of this waxing and waning of tidal energy in conjunction with the 18.6 year tidal cycle to influence biological processes from monthly up to inter-annual and inter-decadal scales. For instance, a strong and sustained phytoplankton bloom might optimally develop under periods of calm winds, strong insolation and large tidal currents, with tidal currents above some threshold value providing nutrient resupply to the euphotic zone through mixing. In any given year these three processes may or may not simultaneously occur. The connection between monthly to decadal periods of tidal current modulations and the biota of the continental shelf ecosystem remains largely unknown. However, the tidal forcing ought to be important for such connections since tides give the largest input to the energy budget of the Bering Sea shelf.

Appendix A: Model for the tidal BBL

The first step in constructing the equations for the tidal bottom boundary layer (BBL) is to assume that velocity is a combination of the zeroth-order geostrophic solution and the first order

solution, which represents changes caused by friction [Munk et al., 1970]. For the zeroth-order, the assumption is that the horizontal velocity does not vary along the vertical direction,

$$\frac{\partial u_0}{\partial t} - fv_0 = -g\frac{\partial \zeta}{\partial x} \tag{1a}$$

$$\frac{\partial v_0}{\partial t} + fu_0 = -g\frac{\partial \zeta}{\partial y} \tag{2a}$$

The first-order velocity is defined by,

$$\frac{\partial u_1}{\partial t} - fv_1 = \frac{\partial}{\partial z}N_z\frac{\partial u_1}{\partial z} \tag{3a}$$

$$\frac{\partial v_1}{\partial t} + fu_1 = \frac{\partial}{\partial z}N_z\frac{\partial v_1}{\partial z} \tag{4a}$$

The total velocity $u = u_0 + u_1$ and $v = v_0 + v_1$ away from the bottom will be expressed by u_0 and v_0 only, while at the bottom, due to friction, $u = 0$, and $v = 0$. Therefore, the boundary conditions for the first-order velocity are

$$u_1 = -u_0, \quad v_1 = -v_0 \quad \text{at} \quad z = 0 \qquad \text{and} \quad u_1 = 0 \quad v_1 = 0 \quad z \to \infty \tag{5a}$$

Thus, the above condition states that the motion for the first-order solution is imparted at the bottom. Thorade [1928] (cf. Defant, 1960; Mofjeld, 1980; and Prandle, 1982) demonstrated that the vertical scale of the BBL depends on the tidal ellipse rotation, and for the clockwise (CW) and counterclockwise (CCW) rotation the two different scales occur. Following Sverdrup [1926] the clockwise q and counterclockwise r components are defined as

$$q = u + iv, \qquad \text{and} \qquad r = u - iv \tag{6a}$$

With the above definition the Cartesian velocity components in terms of the CW and CCW components can be written as

$$u = \frac{q+r}{2}, \qquad \text{and} \qquad v = \frac{q-r}{2i} \tag{7a}$$

Equations of motion (3a) and (4a) can be redefined for q and r components by multiplying the second equation by i and taking a sum and a difference,

$$\frac{\partial q_1}{\partial t} + ifq_1 = \frac{\partial}{\partial z} N_z \frac{\partial q_1}{\partial z} \tag{8a}$$

$$\frac{\partial r_1}{\partial t} - ifr_1 = \frac{\partial}{\partial z} N_z \frac{\partial r_1}{\partial z} \tag{9a}$$

Here $q_1 = u_1 + iv_1$ and $r_1 = u_1 - iv_1$. The boundary conditions (5a) need to be reformulated for the rotating components, and the boundary condition at the free surface ought to be changed since the distance from the bottom to the free surface is finite. At the free surface we assume a zero stress condition,

$$\frac{\partial q_1}{\partial z} = 0 \qquad \text{and} \qquad \frac{\partial r_1}{\partial z} = 0 \qquad \text{at} \qquad z = H \tag{10a}$$

At the bottom the total velocity vanishes and the first-order velocity is defined by the zero-order velocity

$$q_1 = -q_0 \qquad \text{and} \qquad r_1 = -r_0 \qquad \text{at} \qquad z = 0 \tag{11a}$$

Here $q_0 = u_0 + iv_0$ and $r_0 = u_0 - iv_0$. Solution to equation (8a) and (9a) for the constant eddy viscosity coefficient N_z and for all dependent variables changing in time as $e^{-i\omega t}$ can be written as [Mofjeld, 1980],

$$q_1 = -q_0 Q \qquad \text{and} \qquad r_1 = -r_0 R \tag{12a}$$

where

$$Q = \frac{\cosh[\alpha_q (z - H)]}{\cosh(\alpha_q H)} \qquad \text{and} \qquad R = \frac{\cosh[\alpha_r (z - H)]}{\cosh(\alpha_r H)} \tag{13a}$$

The total velocity is defined as

$$q = q_0 + q_1 = q_0 (1 - Q) \qquad \text{and} \qquad r = r_0 + r_1 = r_0 (1 - R) \tag{14a}$$

Here

$$\alpha_q = (1+i)[(f-\omega)/2N_z]^{1/2}, \quad \text{if} \quad \omega < f$$

$$\alpha_q = (1-i)[(\omega-f)/2N_z]^{1/2}, \quad \text{if} \quad \omega > f \tag{15a}$$

$$\alpha_r = (1-i)[(\omega+f)/2N_z]^{1/2}, \quad \text{for all} \quad \omega, \quad \text{and} \quad f > 0 \tag{16a}$$

Description of the vertical exchange of momentum in the uniform and density-stratified water columns is achieved better through the depth-dependent eddy viscosity. The first step is to solve equations for temperature (T) and salinity (S)

$$\frac{\partial T}{\partial t} = \frac{\partial}{\partial z} D_z \frac{\partial T}{\partial z}, \qquad \text{and} \qquad \frac{\partial S}{\partial t} = \frac{\partial}{\partial z} D_z \frac{\partial S}{\partial z}, \tag{17a}$$

to define the density (ρ) distribution along the vertical direction.

In the eddy viscosity parameterization we follow the approach by Galperin et al. [1988]. The eddy viscosity (N_z) and eddy diffusivity (D_z) are computed according to

$$N_z = lqS_M \qquad \text{and} \qquad D_z = lqS_H \tag{18a}$$

Where l is the mixing length, q the square root of twice the kinetic energy, and S_M and S_H are functions of the vertical stratifications. The definition of these functions is given in Blumberg and Mellor [1987] and Galperin et al. [1988]. The equation for the turbulent energy

$$\frac{\partial q}{\partial t} = 2N_z[(\frac{\partial u}{\partial z})^2 + (\frac{\partial v}{\partial z})^2] + 2D_z \frac{g}{\rho}\frac{\partial \rho}{\partial z} - \frac{2q^3}{B_1 l} \tag{19a}$$

and the equation for the length l

$$\frac{\partial q^2 l}{\partial t} = lE_1 N_z[(\frac{\partial u}{\partial z})^2 + (\frac{\partial v}{\partial z})^2] + lE_2 D_z \frac{g}{\rho}\frac{\partial \rho}{\partial z} - \frac{q^3}{B_1}\tilde{W} \tag{20a}$$

complete the turbulence closure. Here $B_1 = 16.6$, E_1=1.8 and E_2=1.33. $\tilde{W}$ defines a wall proximity function, see formulas (13) and (14) in Blumberg and Mellor [1987].

Acknowledgments:

First and foremost, the authors wish to thank the investigators whose data were graciously made available for the analyses in this study and who offered many helpful suggestions to early drafts of this manuscript. The bulk of the data used in this manuscript are from a study designed to investigate dense water formation within the St. Lawrence Island polynya and the subsequent migration away from the polynya area. Knut Aagaard, Jens Meincke, Detlef Quadfasel and Tom Weingartner all provided RCM data. Special appreciation is directed to Tom Weingartner who provided the ADCP data and offered much guidance with the analyses. For the field program, thanks are extended to mooring technicians Jim Johnson, David Leech, Andreas Welsch and Ulrich Druebbisch as well as the captain and crew of the R/V Alpha Helix, all of whom contributed to the successful deployment and recovery efforts. We thank the residents of the village of Gambell who assisted us on a number of instances during both the deployment and the recovery field campaigns. Finally, we would like to thank both anonymous reviewers for their comments and suggestions to help make this a stronger manuscript. Seth Danielson was supported through NSF grant OCE 9730697.

References:

Baines, P.G., Boyer, D.L. and Xie, B. (2004), Laboratory simulations of coastally trapped waves with rotation, topography and stratification, Submitted to *Dynamics of Atmospheres and Oceans.*

Blumberg, A. F., and G. L. Mellor (1987), A description of a three-dimensional coastal ocean model, In *Three-Dimensional Coastal Models*, edited by N. S. Heaps, AGU, 1-16.

Coachman, L. K. (1986), Circulation, water masses, and fluxes on the southeastern Bering Sea shelf, *Cont. Shelf Res., 5*, 23-108.

Coachman, L. K., K. Aagaard, and R. B. Tripp (1975), *Bering Strait: The Regional Physical Oceanography*, University of Washington Press, Seattle, WA, 172 pp.

Defant, A. (1960), *Physical Oceanography*, Pergamon Press, 2, 598 pp (see page 326).

Emery, W.J., and R.E. Thomson (2001), *Data Analysis Methods in Physical Oceanography*, 2nd and Revised Edition, Elsevier, Amsterdam, 638 pp.

Fjeldstad, J. E. (1936), *Results of Tidal Observations*, The Norwegian North Polar Expedition with the "Maud" 1918–1925, Scientific Results, v. IV, No. 4, Bergen, 3–57.

Foldvik, A., J. H. Middleton, and T. D. Foster (1990), The tides of the southern Weddel Sea, *Deep-Sea Research, 37, 8*, 1345–1362.

Foreman, M. G. G., and R. F. Henry (1989), The harmonic analysis of tidal model time series, *Adv. Water Resources, 12*, 109–120.

Galperin, G., L.H. Kantha, S. Hassid, and A. Rossati (1988), A quasi-equilibrium turbulent energy model for geophysical flows, *J. Atmosph. Sciences, 45, 1*, 55–62.

Gonella, J. (1972), A rotary-component method for analysing meteorological and oceanographic vector time series, *Deep-Sea Res., 19*, 833-846.

Hood, D. W., and J. A. Calder, eds. (1981), *The Eastern Bering Sea Shelf: Oceanography and Resources, Vols I and II*, Office of Marine Pollution Assessment, NOAA, 1339 pp.

Howarth, M. J. (1998), The effect of stratification on tidal current profiles, *Cont. Shelf Res., 18,* 1235-1254.

Johnson, W., and Z. Kowalik (1986), Modeling of storm surges in the Bering Sea and Norton Sound, *J. Geophys. Res. 91(C4)*, 5119-5128.

Kantha, L. H. (1995), Barotropic tides in the global oceans from a nonlinear tidal model assimilating altimetric tides, 1. Model description and results, *J. Geophys. Res., 100*, 25,283-25,308.

Kowalik, Z. (1999), Bering Sea Tides, in: *Dynamics of The Bering Sea: A summary Physical, Chemical and Biological Characteristics, and a Synopsis of Research on the Bering Sea*, edited by Loughlin, T. R., and K. Ohtani, Alaska Sea Grant Press, Fairbanks, AK, 93–127.

Kowalik Z., and A. Yu. Proshutinsky (1994), The Arctic Ocean Tides, in: *The Polar Oceans and Their Role in Shaping the Global Environment: Nansen Centennial Volume*, *Geoph. Monograph 85*, edited by Johanessen, O. M., R. D. Muench, and J. E. Overland, AGU, 137-158.

Maas, L. R. M., and J. J. M. van Haren (1987), Observations on the vertical structure of tidal and inertial currents in the central North Sea, *J. Mar. Res., 45, 2*, 293-318.

Marchuk, G. I., and B. A. Kagan (1977), *Oceanic Tides*, Gidrometizdat. Leningrad, 296 pp.

Mofjeld, H. O. (1980), Effects of vertical viscosity on Kelvin waves, *J. Phys. Oceanogr., 10*, 1039-1050.

Mofjeld, H. O. (1984), *Recent observations of tides and tidal currents from the northeastern Bering Sea shelf*, NOAA Tech. Memo. ERL PMEL-57, PMEL, Seattle, 36 pp.

Mofjeld, H.O. (1986), Observed tides on the northeastern Bering Sea shelf, *J. Geophys. Res., 91 (C2)*, 2593-2606.

Mofjeld, H. O., J. D. Schumacher, and D. J. Pashinski (1984), *Theoretical and observed profiles of tidal currents at two sites on the southeastern Bering sea shelf*, NOAA Tech. Memo. ERL, PMEL-62, PMEL, Seattle, 60 pp.

Mooers, C.N.K. (1973), A technique for the cross spectrum analysis of pairs of complex-valued time series, with emphasis on properties of polarized components and rotational invariants, *Deep-Sea Res., 20*, 1129-1141.

Munk, W., F. Snodgrass, and M. Wimbush (1970, Tides off-shore: Transition from California coastal to deep-sea waters, *Geop. Fluid Dyn., 1*, 161-235.

Niebauer, H. J., N. A. Bond, L. P. Yakunin, and V. V. Plotnikov (1999), An Update on the Climatology and Sea Ice of the Bering Sea, in: *Dynamics of The Bering Sea: A summary Physical, Chemical and Biological Characteristics, and a Synopsis of Research on the Bering Sea*, edited by Loughlin, T. R., and K. Ohtani, Alaska Sea Grant Press, Fairbanks, AK, 29-59.

Pawlowicz, R., B. Beardsley, and S. Lentz (2002), Classical tidal harmonic analysis including error estimates in MATLAB using T_TIDE, *Computers and Geosciences 28*, 929-937.

Pearson, C. A., H. O. Mofjeld, and R. B. Tripp (1981), Tides of the Eastern Bering Sea shelf, in: *The Eastern Bering Sea Shelf: Oceanography and Resources*, edited by Hood D. W., and J. A. Calder, US Dept. of Commerce, 111-130.

Pease, C.H., and P. Turet (1989), Sea ice drift and deformation in the Western Arctic, *EEE Publ. N. 89CH2780/5*, 1276-1281.

Prandle, D. (1982), The vertical structure of tidal current, *Geophys. Astrophys. Fluid Dyn., 22*, 22-49.

Pugh, D. T. (1987), *Tides, Surges and Mean Sea-Level*, John Wiley & Sons, 472 pp.

Schumacher, J. D., K. Aagaard, C.H. Pease, and R.B. Tripp (1983), Effects of a shelf polynya on flow and water properties in the northern Bering Sea, *J. Geophys. Res., 88, No. C5*, 2723-2732.

Souza, A. J., and J. H. Simpson (1996) Interaction between mean water column stability and tidal shear in the production of semi-diurnal switching of stratification in the Rhine ROFI, In: *Coastal and Estuarine Studies , 53*, AGU, 83-96.

Sünderman, J. (1977), The semidiurnal principal lunar tide M_2 in the Bering Sea, *Deutsche Hydrog. Zeitschrift, 30*, 91-101.

Sverdrup, H. U. (1926), Dynamics of tides on the North-Siberian shelf, *Geofys. Publ. Norske Videnskaps-Akad., 4, 5*, Oslo, 1-75.

Thorade, H. (1928), Gezeitenuntersuchungen in der Deutschen Bucht der Nordsee, *Deutsche Seewarte, 46, 3*, 85 pp.

van Haren, H. (2000), Properties of vertical current shear across stratification in the North Sea, *J. Mar. Res., 58, 2*, 465-491.

Visser, A. W., A. J. Souza, K. Hessner, and J. H. Simpson (1994), The effect of stratification on tidal current profiles in the region of freshwater influence, *Oceanologica Acta, 17, 4*, 369-381.

Table Captions:

Table 1. Basic environmental components of the St. Lawrence Island region and their approximate annual distributions. Shaded boxes denote nominal months of influence by relevant processes.

Table 2. Mooring names, locations, water column depth, instrument depth, instrument type and record lengths are given. Historical mooring names and parameters (Pearson et al., 1981; Mofjeld, 1984) are denoted with italics. RCM = Aanderaa RCM-4 and RCM-7 instruments, ADCP = RD Instruments 300 KHz Acoustic Doppler Current Profiler.

Table 3. Tidal parameters derived from overlapping 29-day analyses of the current meter records from the St. Lawrence Island region and from the barotropic model. Given are semi-major and semi-minor ellipse axes (cm/s), rotation direction (CW=clockwise, CCW=counterclockwise), the phase angle (degrees) referred to Greenwich and the inclination (degrees) of the semi-major axis referenced in a counter-clockwise fashion from due east. Mean and standard deviations are computed with respect to the ensemble of 29-day analyses, beginning 15 days from the start of the record. Historical mooring names and parameters (Pearson et al., 1981; Mofjeld, 1984) are denoted with italics. Model parameters that fall within the 95% confidence limits of the observed parameters are shaded with boldface type. “VA” in the depth column for F6 and F8 refer to analysis of vertically averaged currents from these two ADCP moorings.

Figure Captions:

Figure 1. Map of the eastern Bering Sea with place names and labeled bathymetric contours. Mooring locations with tidal analyses new to this study are marked with squares and historical mooring locations are marked with circles.

Figure 2. M_2 observed and estimated tidal ellipses. Red ellipses are from the model, blue ellipses are from the current meter records. Every fifth model grid point is displayed.

Figure 3. K_1 tidal ellipses, depicted as in Figure 2.

Figure 4. Vertical profiles of velocity parameters from year-long analysis at mooring F8, for M_2 (heavy lines) and K_1 (light lines) tidal currents. Dotted lines depict the ±95% confidence limits for each parameter. Positive (negative) sign of the semi-minor axis denotes counterclockwise (clockwise) rotation.

Figure 5. Contours of harmonic constants for the M_2 currents at mooring F8 from September 1998 to September 1999. Shown are: semi-major axis (5a), semi-minor axis (5b), inclination (5c) and Greenwich phase (5d). The horizontal axes denote the month of the year, the vertical axes denote depth through the water column.

Figure 6. Semi-annual modulation due to constituents K_1 and P_1 at mooring F8. The envelope shown indicates the range of current speeds seen on a daily basis.

Figure 7. Rotary power spectra of the currents at mooring F8. Panels depict spectra from a) Winter, 10m depth; b) Winter, 43m depth; c) Summer, 10m depth; and d) Summer, 43m depth. Red (blue) traces correspond to CW (CCW) rotation. Vertical green line locates the inertial period (f).

Figure 8. Vertical structure of the magnitude of the tidal current with constant eddy viscosity coefficient. Thick lines depict M_2 currents and thin lines are for K_1. Solid (dashed) lines denote CCW (CW) rotation.

Figure 9. Vertical structure of the magnitude of a) the M_2 tidal current and b) the K_1 tidal current. Solid (dashed) lines denote CCW (CW) rotation. Thin (thick) lines correspond to constant (variable) eddy viscosity.

Figure 10. Vertical structure of the eddy viscosity coefficient for the CW (continuous line) and CCW (dashed line) motion in the M_2 wave.

Figure 11. Vertical structure of the a) density (σ_t), b) eddy viscosity coefficient and c) magnitude of the velocity for the M_2 wave. For comparison purposes, velocity profiles with stratification (solid) and without stratification (dashed) are both given in 11c.

Figure 12. M_2 tidal ellipses at mooring F8 during the summer period. Calculations are given by broken lines, observations by continuous lines. Depth is shown as distance from the free surface.

Figure 13. Two-day averages of tidal kinetic energy and percent of the total energy accounted for by the tidal currents at F8. Prominent features are 1) enhanced energy during the summer months and 2) monthly beats due to M_2-N_2 superposition.

Table 1.

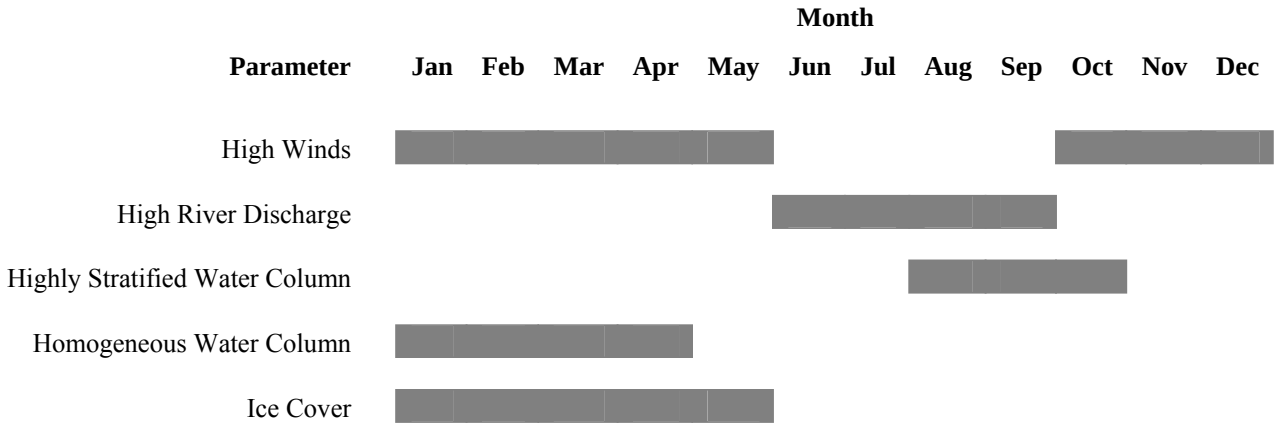

Table 1. Basic environmental components of the St. Lawrence Island region and their approximate annual distributions. Shaded boxes denote nominal months of influence by relevant processes.

Table 2.

Mooring Name	Latitude (° N)		Longitude (° W)		Water Depth (m)	Instr. Depth (m)	Instr. Type	Record Length (hr)
P1	63	12.979	-170	55.155	33	29	RCM	8760
P2	63	6.348	-170	10.521	33	28	RCM	8760
F3	62	56.370	-170	19.958	44	40	RCM	8760
F4	62	55.239	-170	33.013	44	40	RCM	8760
F5	62	52.044	-170	22.982	45	41	RCM	8760
F6	63	9.052	-171	3.955	44	39	ADCP	8760
FTS8	63	0.932	-171	15.842	50	45	RCM	8760
F8	63	1.032	-171	15.591	50	45	ADCP	8760
H1	63	9.726	-172	10.047	60	22	RCM	8760
H1	63	9.726	-172	10.047	60	55	RCM	8760
H3	62	35.077	-171	35.151	48	43	RCM	8760
H3	62	35.077	-171	35.151	48	20	RCM	8760
H4	62	26.243	-170	49.686	42	24	RCM	8760
H4	62	26.243	-170	49.686	42	37	RCM	8760
H5	62	40.039	-170	0.053	42	37	RCM	8760
H5	62	40.039	-170	0.053	42	24	RCM	8760
NC19B	*63*	*58.000*	*-172*	*1.000*	*55*	*45*	*RCM*	*5496*
NC25A	*63*	*0.000*	*-170*	*58.000*	*46*	*36*	*RCM*	*5496*
NC26A	*63*	*11.000*	*-173*	*8.000*	*67*	*57*	*RCM*	*5496*
LD2	*63*	*13.000*	*-168*	*35.000*	*28*	*24*	*RCM*	*696*
LD3	*64*	*0.000*	*-168*	*0.000*	*37*	*33*	*RCM*	*696*

Table 2. Mooring names, locations, water column depth, instrument depth, instrument type and record lengths are given. Historical mooring names and parameters (Pearson et al., 1981; Mofjeld, 1984) are denoted with italics. RCM = Aanderaa RCM-4 and RCM-7 instruments, ADCP = RD Instruments 300 KHz Acoustic Doppler Current Profiler.

Table 3a.

Constituent M_2		Semi-Major Axis (cm/s)			Semi-Minor Axis (cm/s)			Rotation		Inclination (degrees)			Greenwich Phase (degrees)		
Name	**Depth (m)**	**Obs. Mean**	**Std. Dev.**	**Model**	**Obs. Mean**	**Std. Dev.**	**Model**	**Obs. Mean**	**Model**	**Obs. Mean**	**Std. Dev.**	**Model**	**Obs. Mean**	**Std. Dev.**	**Model**
P1	29	6.7	1.5	**7.0**	1.3	0.7	**1.3**	CCW	**CCW**	148	9	156	74	7	**76**
P2	28	7.2	1.3	**6.8**	2.8	1.3	0.7	CCW	**CCW**	134	8	**130**	50	8	30
F3	40	11.5	3.6	**12.5**	1.5	0.9	0.0	CCW	**CCW**	137	4	142	53	5	**56**
F4	40	10.1	3.3	**10.2**	0.9	0.8	0.4	CCW	CW	143	6	**145**	58	6	63
F5	41	10.6	3.7	**11.7**	0.9	0.9	**0.8**	CCW	CW	145	7	**146**	54	5	**57**
F6	10	16.0	2.0	7.7	3.5	1.2	1.0	CW	CCW	164	6	159	65	6	83
F6	VA	13.7	1.0	7.7	1.3	0.2	1.0	CW	CCW	159	2	**159**	59	1	83
F6	37	9.9	1.6	7.7	2.2	0.8	1.0	CCW	**CCW**	147	13	159	41	12	83
FTS8	45	8.3	2.3	**7.8**	0.4	0.6	**0.5**	CW	**CW**	133	7	150	69	8	84
F8	10	15.0	1.0	7.8	3.9	0.8	0.5	CW	**CW**	154	5	150	60	3	84
F8	VA	14.3	1.2	7.8	3.3	0.4	0.5	CW	**CW**	152	4	**150**	57	2	84
F8	43	10.5	1.3	7.8	0.1	0.8	**0.5**	CCW	**CW**	146	9	**150**	45	8	84
H1	22	8.7	2.7	**8.6**	2.5	1.1	**1.9**	CW	**CW**	143	2	124	115	5	**116**
H1	55	7.1	1.9	8.6	0.0	0.5	1.9	-	**CW**	136	8	124	100	8	116
H3	20	7.1	2.7	**7.3**	3.9	1.5	**4.7**	CW	**CW**	162	9	153	72	5	60
H3	43	6.2	2.4	**7.3**	2.8	1.3	4.7	CW	**CW**	159	5	153	60	6	**60**
H4	24	8.0	2.9	**8.2**	3.8	1.5	**3.9**	CW	**CW**	172	4	165	51	4	44
H4	37	8.3	2.4	**8.2**	3.0	1.4	3.9	CW	**CW**	169	6	165	42	7	**44**
H5	24	12.2	2.7	15.3	2.1	0.9	**2.4**	CW	**CW**	9	3	160	229	8	48
H5	37	10.9	3.6	15.3	0.3	1.0	2.4	CW	**CW**	179	7	160	220	8	48
NC19B	*45*	*5.3*	*0.4*	*13.0*	*0.6*	*0.5*	***0.8***	*CCW*	*CW*	*28*	*8*	***32***	*190*	*12*	*202*
NC25A	*36*	*4.8*	*0.7*	*11.8*	*0.2*	*0.5*	*1.1*	*CCW*	***CW***	*151*	*5*	*79*	*242*	*6*	*120*
NC26A	*57*	*3.1*	*0.7*	*7.9*	*1.1*	*0.4*	*0.3*	*CCW*	*CW*	*101*	*4*	*134*	*104*	*5*	***107***
LD2	*24*	*15.4*		*6.0*	*8.5*		*2.6*	*CCW*	*CW*	*59*		*106*	*130*		*128*
LD3	*33*	*4.9*		*8.2*	*3.5*		*0.3*	*CCW*	*CW*	*128*		*149*	*78*		*76*

Table 3. Tidal parameters derived from overlapping 29-day analyses of the current meter records from the St. Lawrence Island region and from the barotropic model. Given are semi-major and semi-minor ellipse axes (cm/s), rotation direction (CW=clockwise, CCW=counterclockwise), the phase angle (degrees) referred to Greenwich and the inclination (degrees) of the semi-major axis referenced in a counter-clockwise fashion from due east. Mean and standard deviations are computed with respect to the ensemble of 29-day analyses, beginning 15 days from the start of the record. Historical mooring names and parameters (Pearson et al., 1981; Mofjeld, 1984) are denoted with italics. Model parameters that fall within the 95% confidence limits of the observed parameters are shaded with boldface type. "VA" in the depth column for F6 and F8 refer to analysis of vertically averaged currents from these two ADCP moorings.

Table 3b.

Constituent K_1		**Semi-Major Axis** *(cm/s)*			**Semi-Minor Axis** *(cm/s)*			**Rotation**		**Inclination** *(degrees)*			**Greenwich Phase** *(degrees)*		
Name	**Depth** *(m)*	**Obs. Mean**	**Std. Dev.**	**Model**	**Obs. Mean**	**Std. Dev.**	**Model**	**Obs. Mean**	**Model**	**Obs. Mean**	**Std. Dev.**	**Model**	**Obs. Mean**	**Std. Dev.**	**Model**
P1	29	2.0	0.7	**1.9**	0.3	0.3	**0.2**	CW	CCW	163	11	154	224	32	**208**
P2	28	2.1	0.6	1.6	0.0	0.3	**0.6**	-	**CW**	152	10	134	187	17	166
F3	40	3.6	1.4	**3.8**	1.1	0.7	0.4	CW	**CW**	156	12	142	208	15	187
F4	40	3.4	1.3	**3.2**	1.2	0.5	0.4	CW	**CW**	156	9	145	207	16	192
F5	41	3.4	1.3	**3.7**	1.1	0.6	0.7	CW	**CW**	159	8	147	205	16	183
F6	10	3.6	0.8	2.3	0.7	0.5	0.2	CW	CCW	150	18	158	199	19	**211**
F6	VA	3.5	0.8	2.3	0.8	0.4	0.2	CW	CCW	155	9	**158**	203	16	**211**
F6	37	3.1	0.7	2.3	0.6	0.5	0.2	CW	CCW	167	10	**158**	213	14	**211**
FTS8	45	3.0	0.8	2.4	0.6	0.3	**0.5**	CW	**CW**	147	7	**150**	223	17	**218**
F8	10	3.9	1.0	2.4	1.4	0.4	0.5	CW	**CW**	142	6	150	199	14	218
F8	VA	3.9	0.9	2.4	1.3	0.4	0.5	CW	**CW**	146	5	150	200	15	218
F8	43	3.5	0.7	2.4	1.0	0.3	0.5	CW	**CW**	158	6	150	208	15	**218**
H1	22	2.6	0.8	**2.9**	0.7	0.3	0.8	CW	**CW**	140	9	127	234	19	**240**
H1	55	2.7	1.0	**2.9**	0.6	0.4	**0.8**	CW	**CW**	154	9	127	245	18	**240**
H3	20	2.7	1.0	**2.9**	1.7	0.7	2.3	CW	**CW**	159	22	3	187	28	334
H3	43	2.7	0.8	**2.9**	1.8	0.7	2.3	CW	**CW**	150	25	3	212	30	334
H4	24	3.2	0.8	**3.1**	2.1	0.7	**2.0**	CW	**CW**	176	20	24	174	26	313
H4	37	3.4	0.9	**3.1**	2.4	0.7	**2.0**	CW	**CW**	15	26	**24**	161	27	313
H5	24	4.1	1.0	5.1	1.6	0.5	2.6	CW	**CW**	21	8	176	344	16	**164**
H5	37	3.8	1.1	5.1	1.6	0.7	2.6	CW	**CW**	22	9	176	352	18	**164**
NC19B	*45*	*3.0*	*0.4*	*5.9*	*0.0*	*0.2*	***0.1***	-	***CW***	*44*	*4*	*33*	*355*	*9*	***350***
NC25A	*36*	*1.8*	*0.4*	*5.9*	*0.4*	*0.2*	*0.1*	*CCW*	***CCW***	*158*	*9*	*74*	*214*	*10*	*322*
NC26A	*57*	*1.3*	*0.2*	*3.1*	*0.7*	*0.2*	*0.3*	*CCW*	*CW*	*146*	*14*	*19*	*219*	*17*	*16*
LD2	*24*	*7.5*		*2.1*	*0.7*		*1.4*	*CW*	*CW*	*79*		*130*	*29*		*230*
LD3	*33*	*4.0*		*2.5*	*1.7*		*0.6*	*CW*	*CW*	*17*		*149*	*24*		*215*

Figure 1.

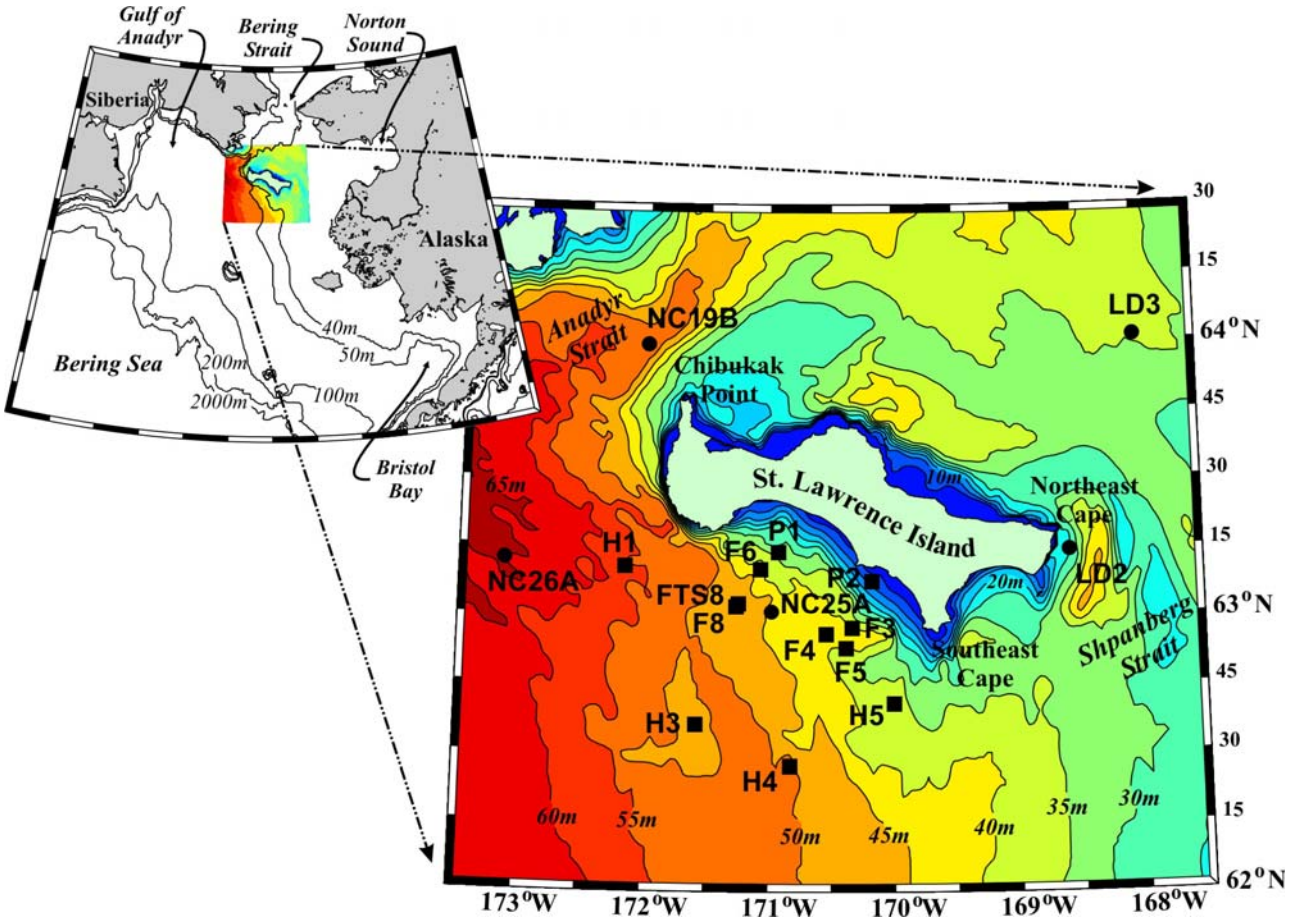

Figure 1. Map of the eastern Bering Sea with place names and labeled bathymetric contours. Mooring locations with tidal analyses new to this study are marked with squares and historical mooring locations are marked with circles.

Figure 2.

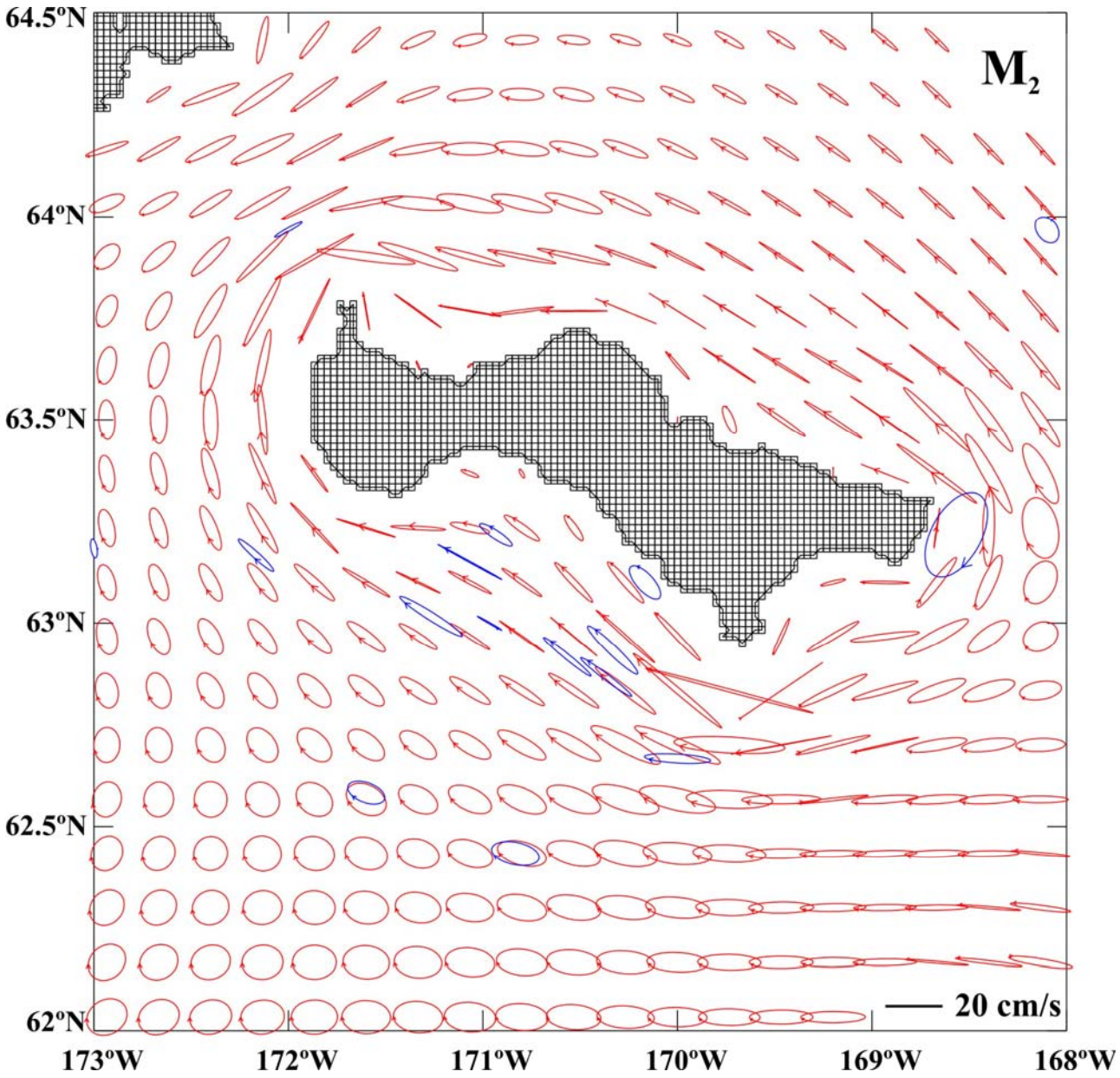

Figure 2. M_2 observed and estimated tidal ellipses. Red ellipses are from the model, blue ellipses are from the current meter records. Every fifth model grid point is displayed.

Figure 3.

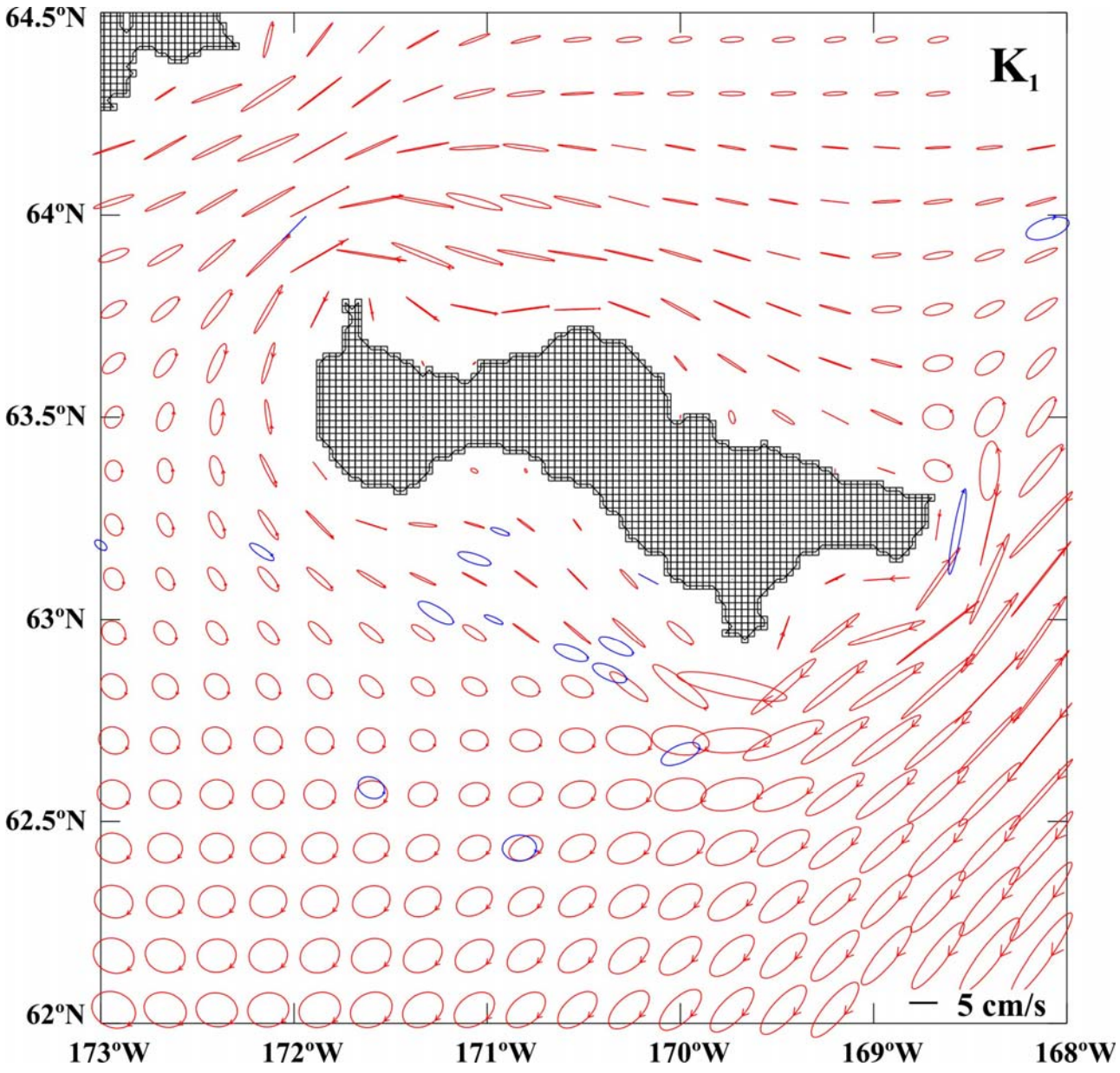

Figure 3. K_1 tidal ellipses, depicted as in Figure 2.

Figure 4.

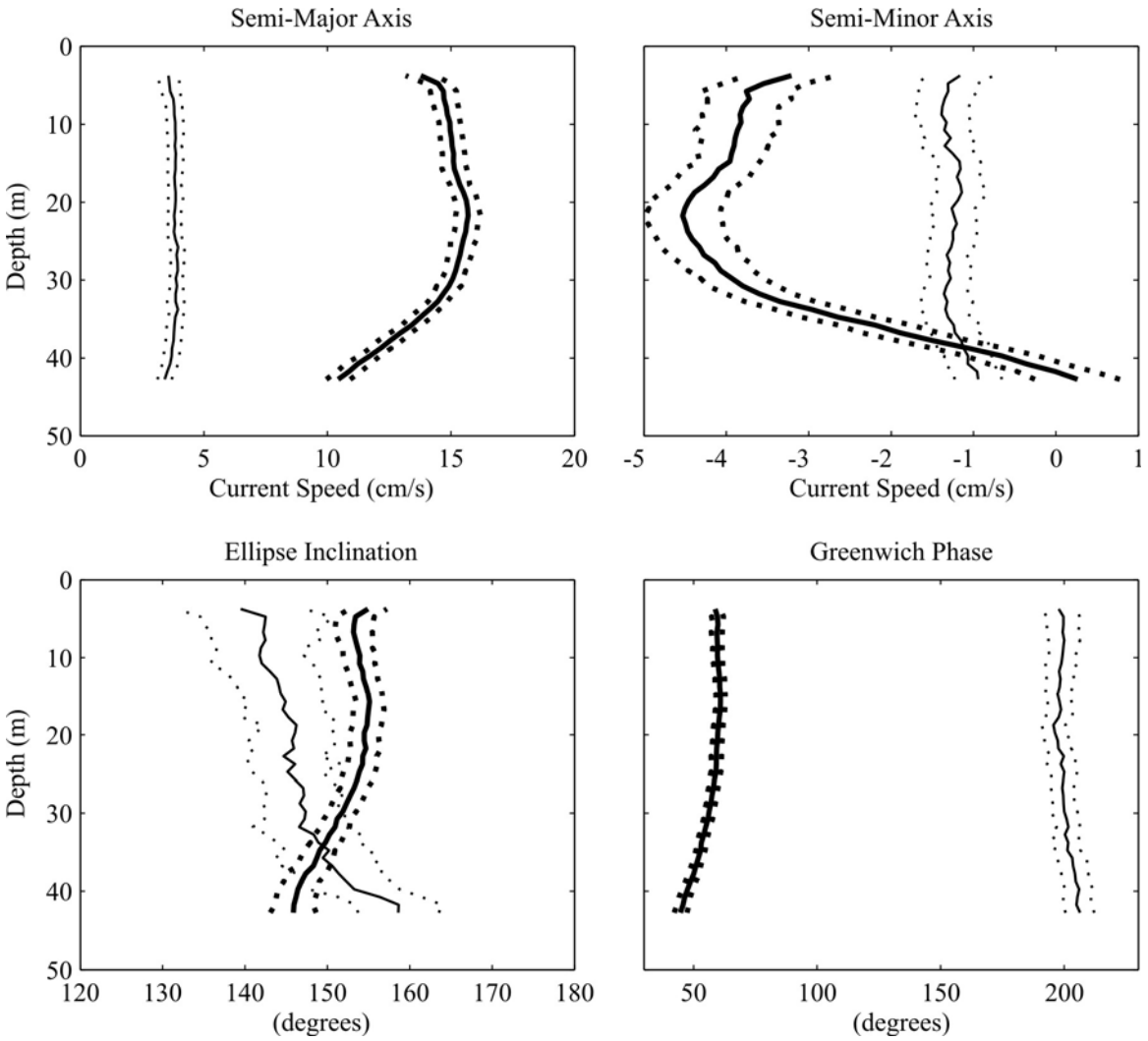

Figure 4. Vertical profiles of velocity parameters from year-long analysis at mooring F8, for M_2 (heavy lines) and K_1 (light lines) tidal currents. Dotted lines depict the ±95% confidence limits for each parameter. Positive (negative) sign of the semi-minor axis denotes counterclockwise (clockwise) rotation.

Figure 5.

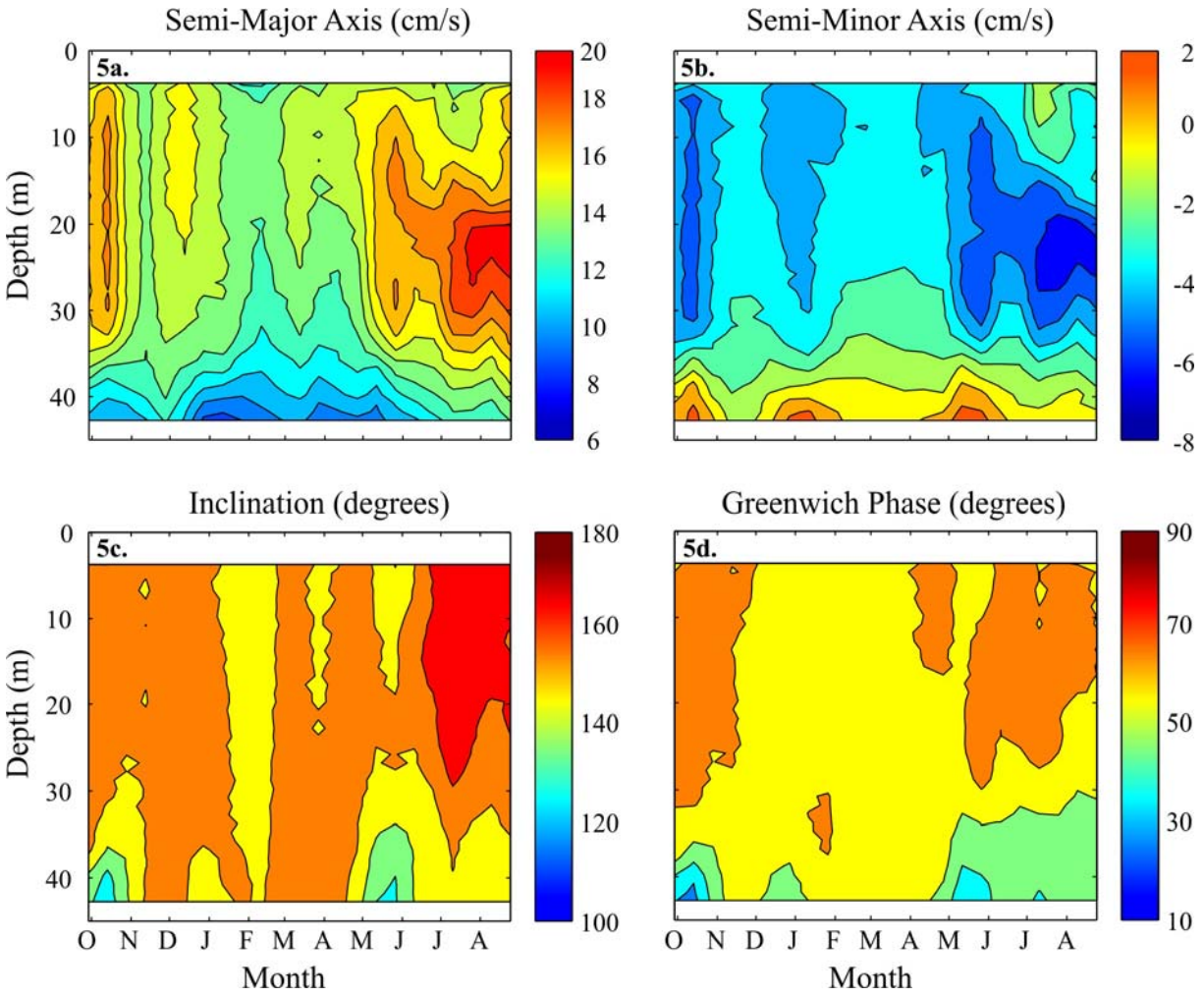

Figure 5. Contours of harmonic constants for the M_2 currents at mooring F8 from September 1998 to September 1999. Shown are: semi-major axis (5a), semi-minor axis (5b), inclination (5c) and Greenwich phase (5d). The horizontal axes denote the month of the year, the vertical axes denote depth through the water column.

Figure 6.

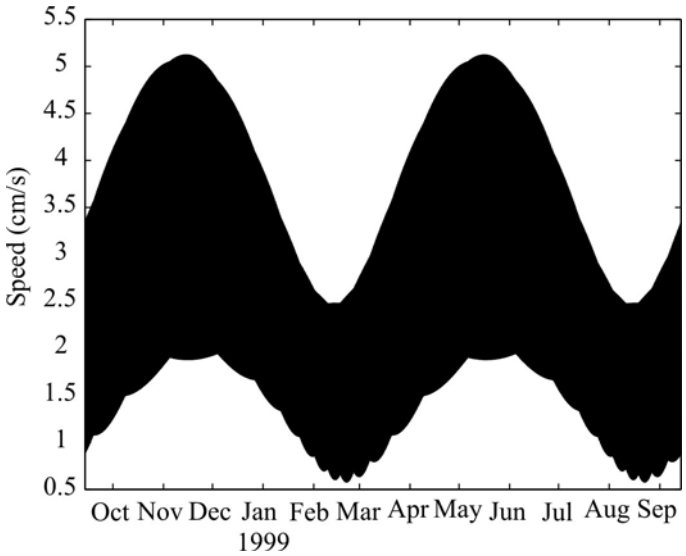

Figure 6. Semi-annual modulation due to constituents K_1 and P_1 at mooring F8. The envelope shown indicates the range of current speeds seen on a daily basis.

Figure 7.

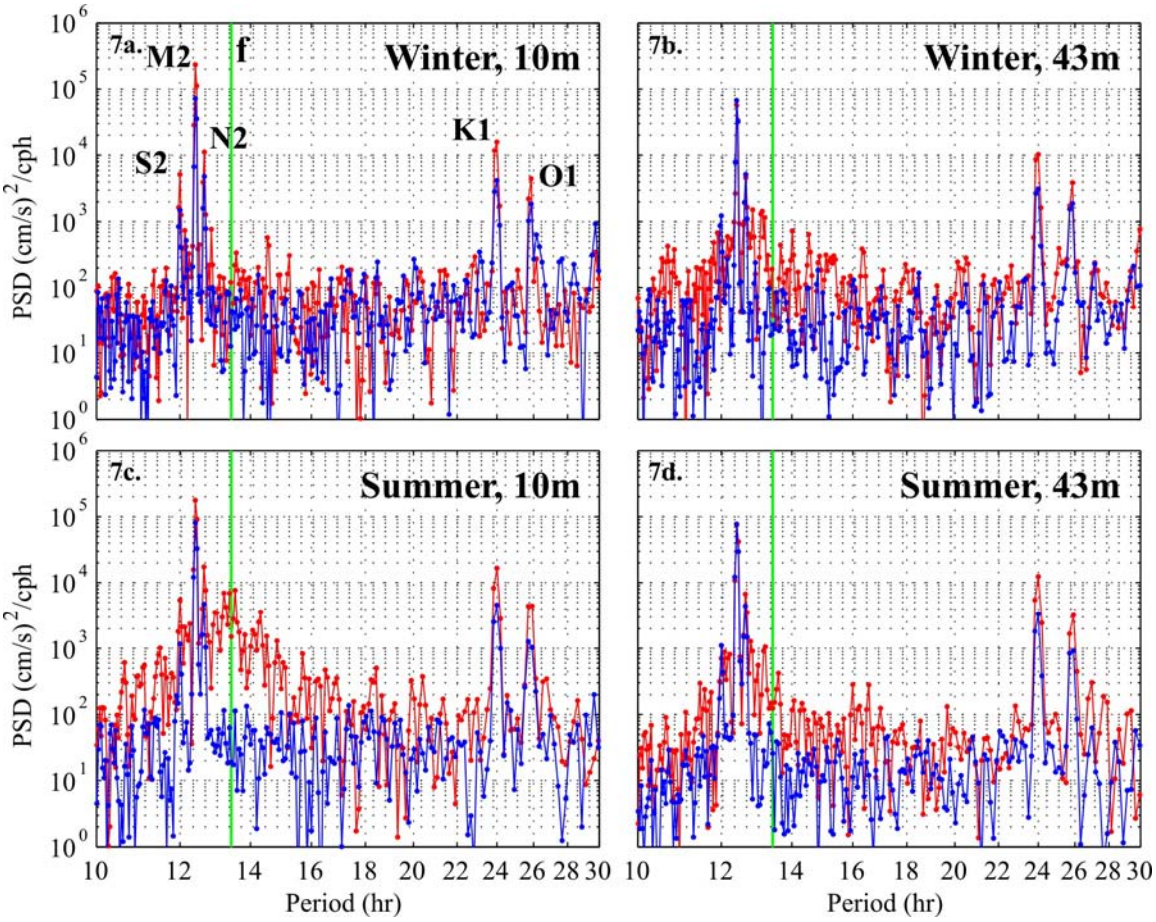

Figure 7. Rotary power spectra of the currents at mooring F8. Panels depict spectra from a) Winter, 10m depth; b) Winter, 43m depth; c) Summer, 10m depth; and d) Summer, 43m depth. Red (blue) traces correspond to CW (CCW) rotation. Vertical green line locates the inertial period (f).

Figure 8.

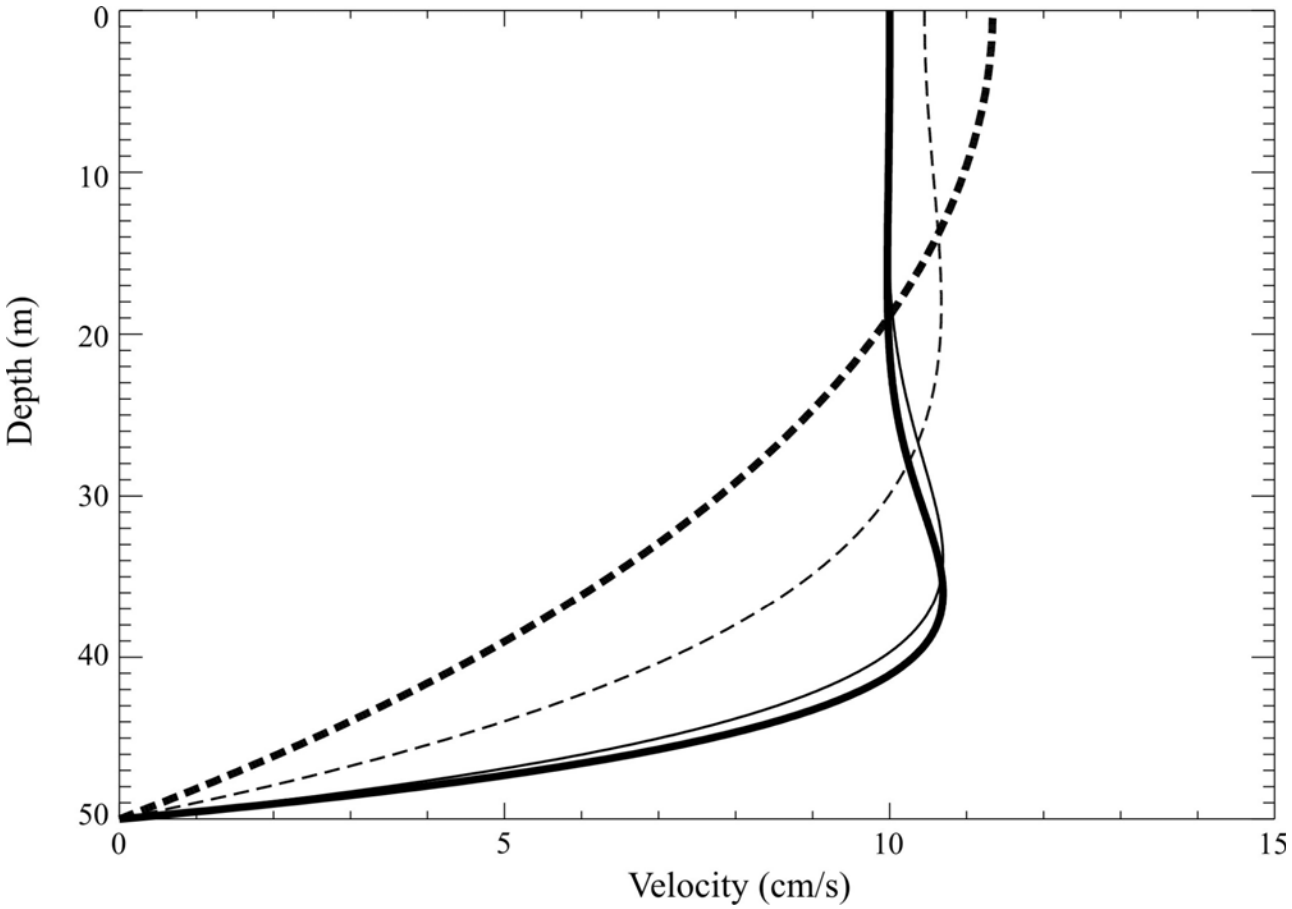

Figure 8. Vertical structure of the magnitude of the tidal current with constant eddy viscosity coefficient. Thick lines depict M_2 currents and thin lines are for K_1. Solid (dashed) lines denote CCW (CW) rotation.

Figure 9.

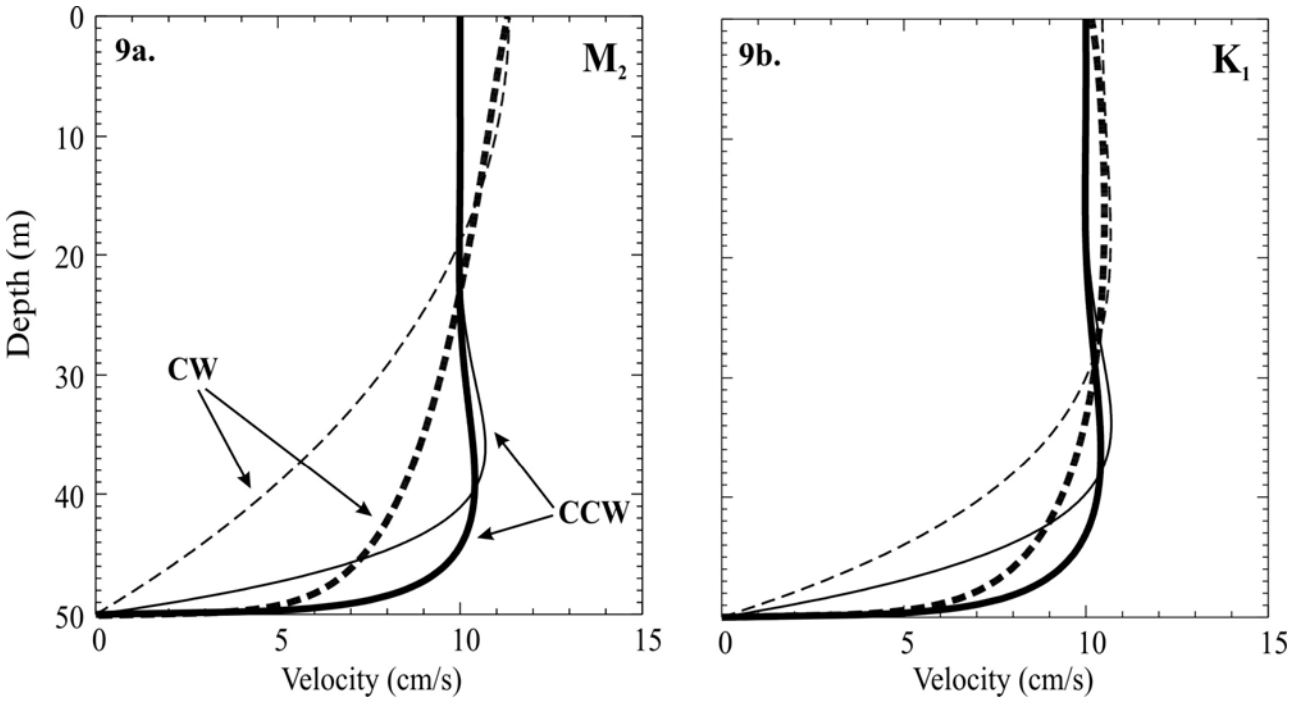

Figure 9. Vertical structure of the magnitude of a) the M_2 tidal current and b) the K_1 tidal current. Solid (dashed) lines denote CCW (CW) rotation. Thin (thick) lines correspond to constant (variable) eddy viscosity.

Figure 10.

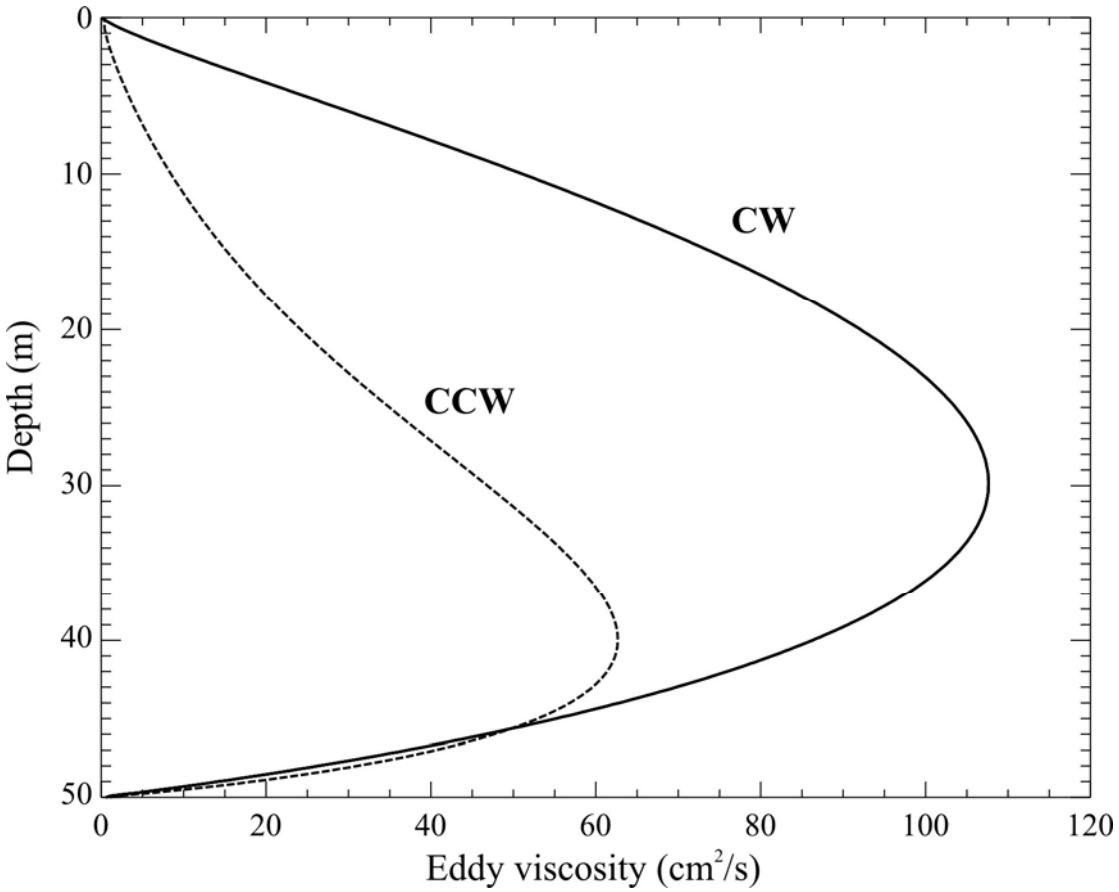

Figure 10. Vertical structure of the eddy viscosity coefficient for the CW (continuous line) and CCW (dashed line) motion in the M_2 wave.

Figure 11.

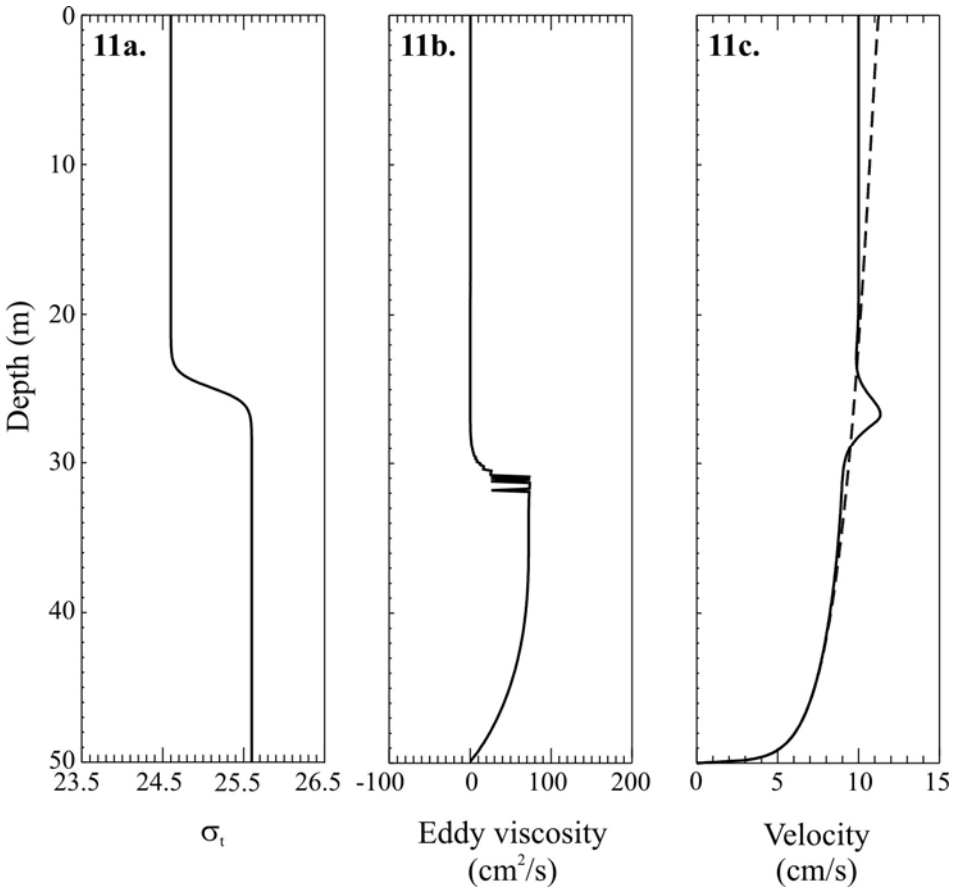

Figure 11. Vertical structure of the a) density (σ_t), b) eddy viscosity coefficient and c) magnitude of the velocity for the M_2 wave. For comparison purposes, velocity profiles with stratification (solid) and without stratification (dashed) are both given in 11c.

Figure 12.

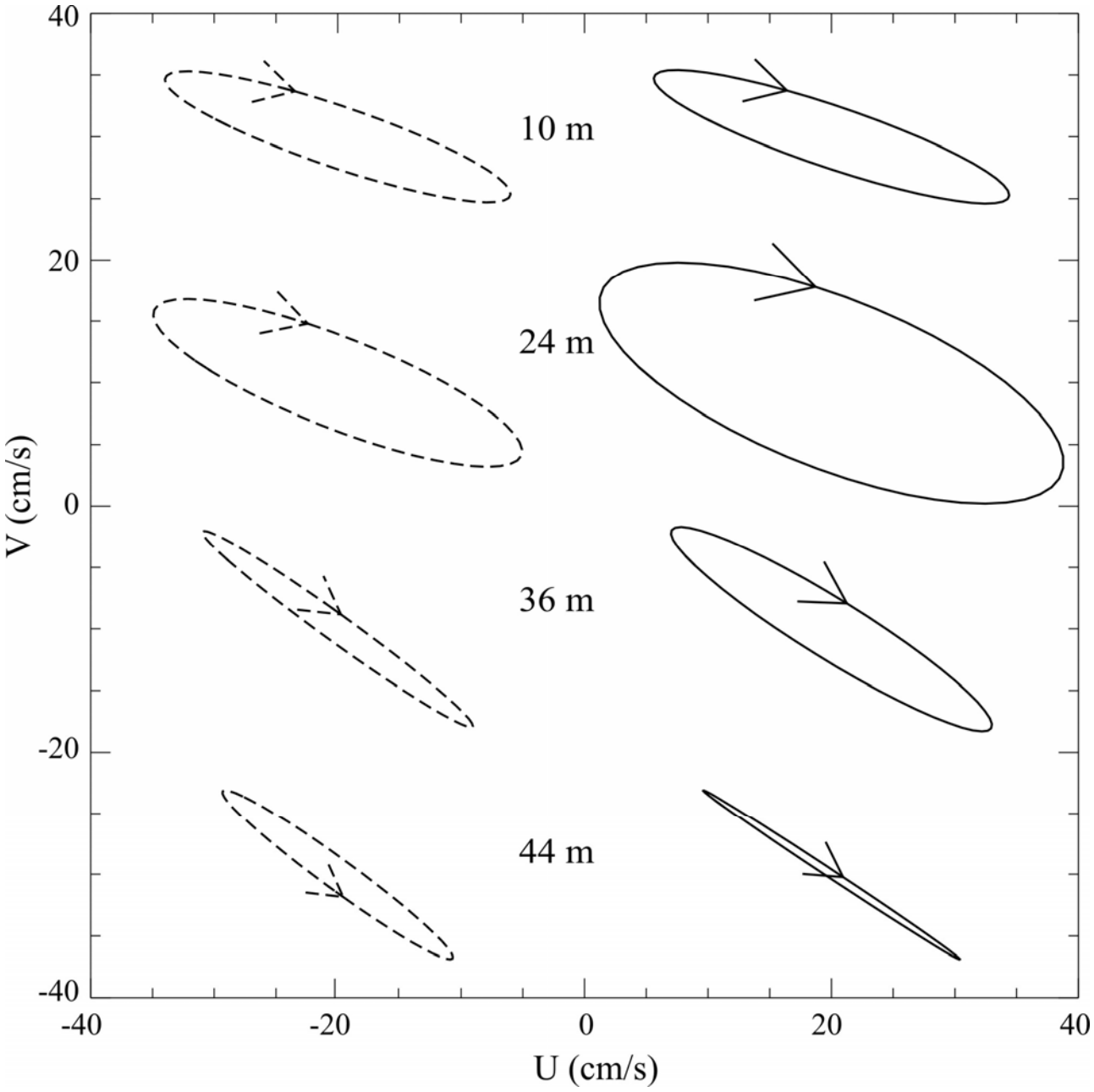

Figure 12. M_2 tidal ellipses at mooring F8 during the summer period. Calculations are given by broken lines, observations by continuous lines. Depth is shown as distance from the free surface.

Figure 13.

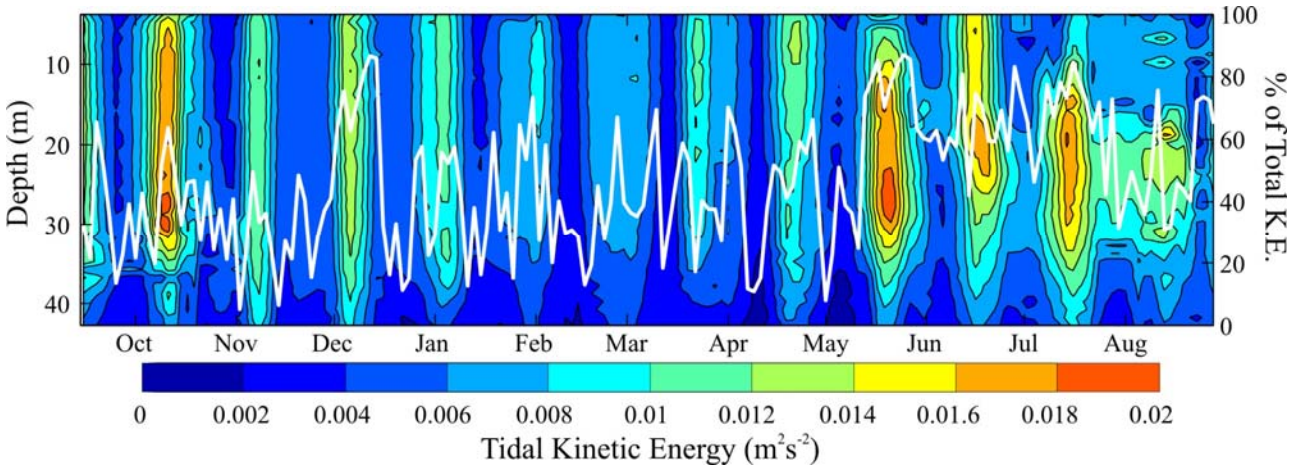

Figure 13. Two-day averages of tidal kinetic energy and percent of the total energy accounted for by the tidal currents at F8. Prominent features are 1) enhanced energy during the summer months and 2) monthly beats due to M_2-N_2 superposition.